UNIVERSITY OF OSLO
Department of Informatics

Linear and nonlinear propagation of limited diffraction beams

Johan-Fredrik
Synnevåg

Cand Scient Thesis

May 1st 1998

Acknowledgment

Contents

Chapter 1

Introduction

1.1 Limited diffraction beam transmission

Medical transducers usually transmit a spherically focused beam, either focused electronically or prefocused by the shape of the transducer, which results in an optimal focusing area. This optimal area is rather small and when moving away from the focusing point, the beam tends to defocus and contrast is lowered. The motivation behind limited diffraction beam transmission, is that these beams have an approximate depth independent shape for a large distance, which would give approximately equal focus through the entire depth of field.

1.2 Nonlinear sound beam distortion

Modern ultrasound systems have the capability to take advantage of nonlinear distortion of soundbeams propagating through tissue. Distortion of the transmitted beam produces energy in higher harmonics, and images are made by receiving the sound beam on the second harmonic, or twice the transmitted frequency. This is referred to as harmonic imaging, and the images often demonstrate improved quality. Quality of ultrasound images depends on the frequency of the transmitted beam and must be chosen high if the objects to be imaged are small. High frequencies are however attenuated more in biological tissue as the beam propagates, leading to reduced depth of penetration inside the objects under study. With harmonic imaging the transmitted frequency is reduced, giving deeper penetration, while still maintaining good resolution since reception is done at a higher frequency.

1.3   Objective of this thesis

The objective of this thesis is to study propagation of limited diffraction Bessel beams and X waves produced by finite bandwidth and aperture and show that good approximations to the exact theoretical beams can be made. Simulation of the Bessel beam has previously been studied at the university, so the main work on linear sound propagation was to develop algorithms for simulating X waves and look at how they could be realized in practice. Both the Bessel beam and X wave are then brought to another area of acoustics, namely propagation under nonlinear conditions, where improved beamprofile is expected on higher harmonics as a result of nonlinear distortion. An algorithm for simulating nonlinear wave propagation from circular symmetric sources is introduced, and simulations from spherically focused beams, Bessel beams and X waves are shown.

Chapter two gives a general introduction to the theory of sound and ultrasound, and chapter three covers the linear wave equation and linear wave propagation, and methods for simulating acoustic fields from finite extent sources under linear conditions. Chapter four and five gives the theoretical background for limited diffraction beams and then looks at how to simulate and realize them in practice. Chapter six looks at wave propagation under nonlinear conditions, by first introducing the nonlinear wave equation and presenting a method for simulating nonlinear acoustic fields, and then simulating nonlinear propagation from limited diffracting sources and comparing them to the spherically focused transducer.

Chapter 2

Sound theory and ultrasound imaging

2.1 Sound

Sound can be regarded as disturbances propagating through a medium. Audible sound is disturbance of air that the human ear can hear and are made by virtually anything that moves. It is made by mechanical vibrations that propagates as a wave by compressing and decompressing the medium which it propagates through. The speed of propagation is dependent on the characteristics of the medium, so different media give different speed of sound. Sound propagates from the source of the mechanical vibrations. If the source is small, the sound beam spreads spherically, meaning that the lines of constant phase (the lines where the propagation distance is the same) are spheres in space as in figure 2.1. Because this is similar to what happens when dropping a stone in water, the lines of constant phase are called wavefronts. If a sensor of about equal spatial extent as the source is far away, the wavefronts are almost straight lines within the extent of the sensor, and the propagating waves can be approximated by plane waves. Plane waves means that the wavefronts are planes in space.

2.1.1 Wavelength

The distance between the wavefronts in figure 2.1 is called wavelength. High frequencies, meaning that the source vibrates rapidly, give small wavelengths, while slower vibrations give greater wavelengths. The wavelength is the distance it takes to propagate one period of a signal, so different media give different wavelengths even if the frequency is the same, since the speed of sound is not equal. In air, where the speed of sound is about 340 m/s, a
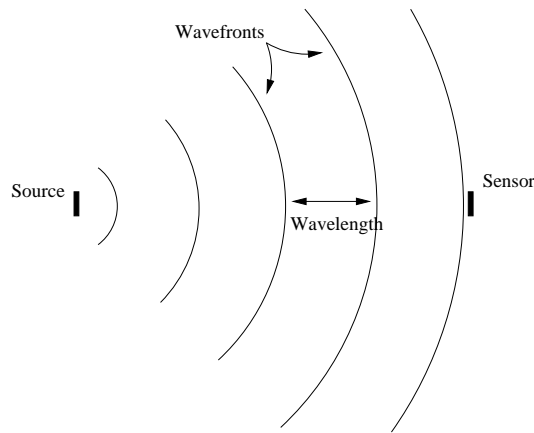
Figure 2.1: Propagating sound beam. The solid lines are wavefronts, and the distance between the wavefronts is the wavelength.

10 KHz source gives 3.4 cm wavelength, while in water where the speed of sound is 1540 m/s, the same source gives 15.4 cm wavelength.

2.1.2   Reflections

When propagating sound hits an object like a wall, part of the energy of the wavefront is reflected off the wall like light on a mirror as shown in figure 2.2. The rest of the energy is absorbed, either by getting lost in the wall or by propagating through to the next room. The amount of energy that is absorbed depends on the material properties of the wall. Medical imaging takes advantage of this phenomenon, by sending short pulses through the body and measuring the reflections.

2.1.3   Diffraction

The acoustic field generated by a source of finite extent is similar to the field of a plane wave traveling through a hole in the wall. When a plane wave, traveling approximately in a straight line, propagates through a hole, it does not continue to propagate as a plane wave, but spreads spherically as shown in figure 2.3. This phenomenon is known as diffraction. It can be explained from Huygen's principle which will be presented later. The amount of diffraction depends on the wavelength and the size of the source, where a larger source gives less diffraction. The size of the source is measured in wavelengths so doubling the frequency is equivalent to doubling the size.

Figure 2.2: (a) Reflections from an object close to the source (b) Reflections from an object where the source is far away. The incoming waves are approximately plane.

Figure 2.3: Sound generated by a finite extent source is similar to a plane wave propagating through a hole.

2.2   Ultrasound

Sound is not just disturbances traveling through air, it also travels through water, earth and the human body, the latter being exploited in ultrasound imaging. While audible sound is in the frequency range of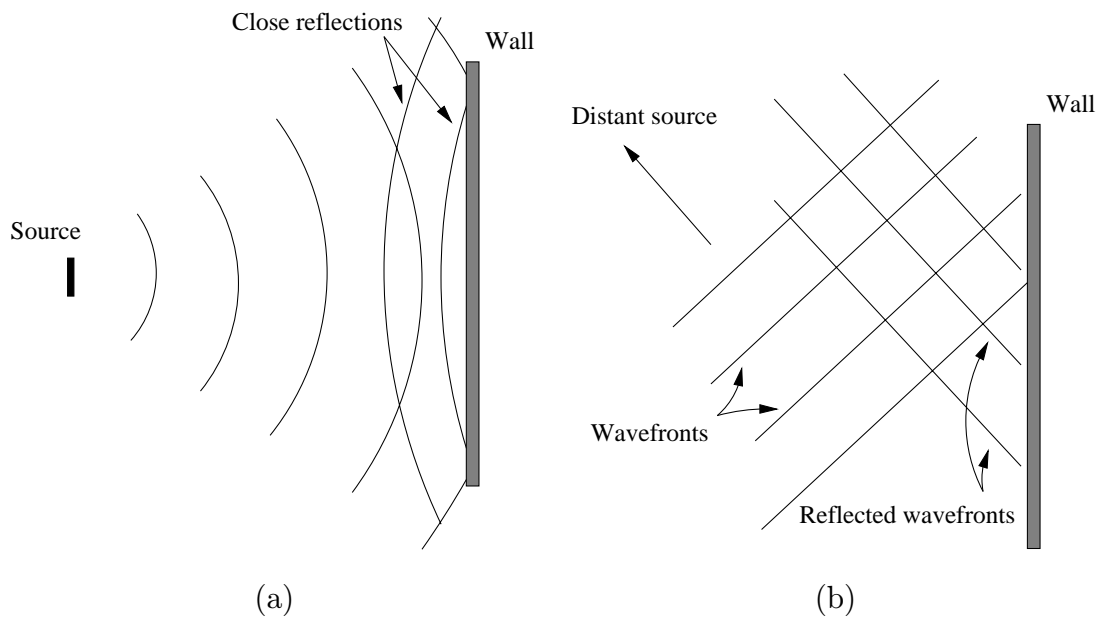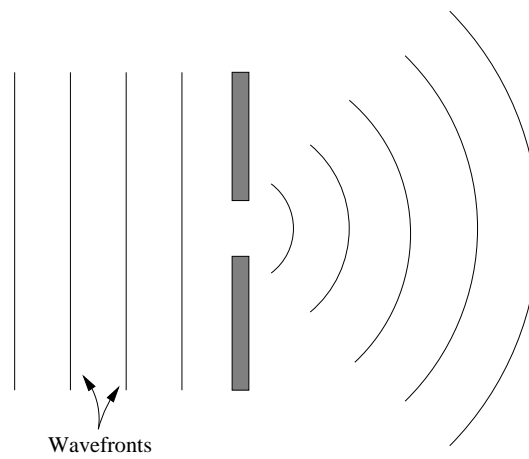 20 Hz - 20 KHz, ultrasound is typically in the range of 2-10 MHz [1]. The resolution of an ultrasound image is dependent on the frequency of the transmitted sound beam. In the previous example the wavelength of a 10 KHz source in water was 15.4 cm which makes it impossible to image small objects. This is one of the reasons why ultrasound frequencies must be used, and low frequencies would also be useless because of diffraction. The size of the transducers in medical ultrasound are only up to a few centimeters, so high frequencies must be used to make them large compared to wavelength. The speed of sound in tissue is about the same as in water, 1540 m/s, and with the frequencies used, the wavelengths are from 0.15 - 0.75 mm. This gives ultrasound beams properties which are similar to light.

Imaging is done by transmitting a short pulse from an ultrasound transducer. Part of the energy of the pulse is reflected when it hits tissue with different characteristics, and the reflected pulse is measured. This is called pulse-echo imaging. An image is constructed by sending pulses in different directions in a plane and measuring the reflections, so the resulting image is a slice through the body.

2.2.1   Resolution

Two important factors in the quality of ultrasound images are lateral and axial resolution. Lateral resolution is the resolution perpendicular to the direction of propagation, and axial resolution is resolution along the sound beam. The axial resolution is usually better than the lateral. To get good axial resolution, the transmitted pulse must be as short as possible. This requires a broadband pulse and therefore a broadband transducer. Ultrasound transducers typically covers 50-80 % of their central frequency.

Lateral resolution is determined by the beamwidth of the transmitted wave. The beamwidth is again determined by the size of the transducer and wavelength. A larger transducer (measured in wavelengths) gives a narrower beam because of diffraction. But the size of the transducer is limited by certain applications. Imaging of the heart is done between the ribs, so the maximum size of the transducer is about 20 mm.

A narrow beam can be accomplished at cost of large sidelobes, but large sidelobes reduce contrast in an image. The contrast is reduced because reflections from the sidelobes interfere with the reflections from the main lobe.
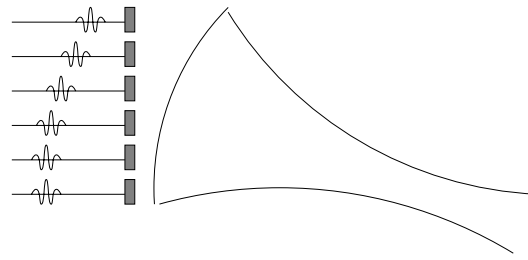
Figure 2.4: Linear phased array. The signals excited from each element are delayed to steer and focus the beam.

Good lateral resolution is accomplished by focusing the transducer at a point at a certain depth. This results in an optimal area where the beam is narrow and the sidelobes are low. The problem is that when moving away from the focusing point, the beam gets broader and the lateral resolution decreases. This is a motivation for transmission of limited diffraction beams, which has approximately the same beam profile over the entire depth of field. The problem with limited diffraction beams are the high sidelobes which are generated. Reflections from these sidelobes would interfere with the reflections from the main lobe, giving reduced contrast and more image artifacts.

2.3 Transducers

Transducers are made of piezoelectric material with electrodes on each side. When the surface is excited by an electrical signal, the material compresses and expands, generating ultrasound energy. The vibrations are transferred to the tissue, and are the source of a soundbeam propagating through the body. Different transducers are available, where different types of linear arrays are the most common. This thesis, which considers zeroth order Bessel beams and X waves, only considers annular arrays, since these sound beams are circular symmetric and require radiation from a two-dimensional plane. The zeroth order beams could therefore not be implemented on linear arrays. Alternatively a two-dimensional array could be used.

2.3.1 Linear phased array

The linear phased array consists of 32-128 elements arranged in a line in one dimension. A beam generated by this transducer can be focused and steered by varying the time delay on each element as shown in figure 2.4.
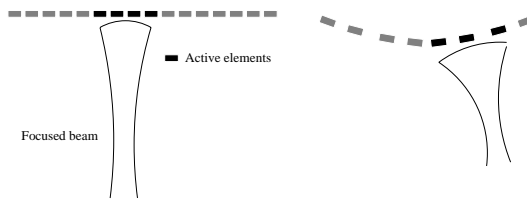
Figure 2.5: Linear switched and linear curved array. Only part of the elements are active at one time.

The focus on transmission is fixed once the beam has left the transducer, but the focusing point can be set manually by the operator. On reception, the time delay is varied dynamically, so that the pulse is always in focus. The signal from each element is then summed. This is known as delay and sum-beamforming. An image is constructed by steering the sound beam in different directions in a one-dimensional plane, giving an image which is narrow in the near-field and broad in the far-field. This is called sectorscan.

2.3.2   Linear switched array and linear curved array

The linear switched array consists of a large number of elements, but only part of the array is used at one time, see figure 2.5. An image is made by transmitting a beam from a subset of the array, and then stepping along the array by selecting a new subset, known as switching. The beam is focused by varying the delay on each element. This is known as linear scan, and gives an image which has the same width in both near- and far-field.

The linear curved array is a curved switched array, and combines the broad image in the far-field of a sectorscan, with the the technology of the switched array.

2.3.3   Annular array

The annular array transducer consists of an array of rings with different radius, see figure 2.6. This array is often prefocused by shaping the transducer spherically, and dynamic focusing on reception is done by varying the time delay on each element, similar to the linear phased array. While the linear array only focuses in the scan plane, the focus of an annular array transducer is the same in all planes. But this array can not be steered electronically. It is steered by wobbling the transducer mechanically in different angles instead of using delays to steer the beam. The advantage of the mechanical wobbling is that the effective aperture size is the same for all angles, while
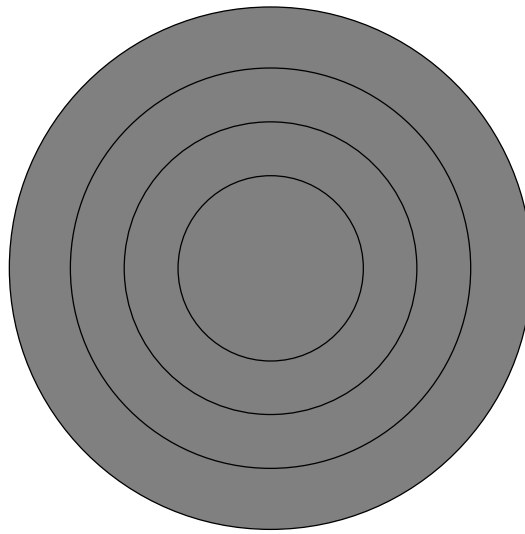
Figure 2.6: 4 element annular array transducer

for electronic steering the effective aperture size is reduced when scanning in angles other than $0°$.

2.3.4 Two-dimensional array

Two-dimensional arrays have elements in both dimensions unlike the linear array which only has elements along a line. This means that this array can be both steered and focused in three dimensions as shown in figure 2.7. The focusing properties would lead to improved image quality, and steering in three dimensions is required for three-dimensional imaging. The disadvantage is that 2D arrays require a large number of elements, and increased number of channels means increased cost of equipment.

2.4 Harmonic imaging

In standard ultrasound imaging, transmission and reception of a beam is done at the same frequency. Harmonic imaging takes advantage of the fact that sound beams generated by high pressure sources are distorted due to nonlinear properties of tissue. As the sound beam propagates, energy is transferred from the fundamental to higher harmonics, and if the initial pressure is high, the energy in the second harmonic is measurable. The sound beam is received at the second harmonic, or twice the transmitted frequency, giving images
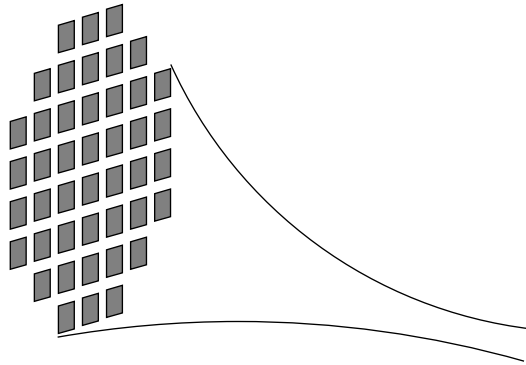
Figure 2.7: A two-dimensional array can be steered and focused in three dimensions.

with better resolution. We know from the previous sections that transmission of higher frequencies gives better resolution. This is also the fact if the high frequencies are generated by nonlinear propagation. The lateral beamwidth is narrower and the sidelobes are lower, giving better resolution and less image artifacts. Since transducers have limited bandwidth, transmission is done at a frequency lower than the central frequency of the transducer which is used for standard imaging, and reception is done at twice the frequency of transmission. An advantage of lower frequency on transmission, is that higher frequencies are attenuated more as the beam propagates, meaning that a lower transmitted frequency will penetrate deeper into the tissue, and also there is less phase aberration at lower transmit frequencies.

Chapter 3

Wave propagation and simulation of acoustic fields

3.1 The three-dimensional wave equation

The physics of wave propagation is well described by the wave equation, so this chapter begins with a derivation of the wave equation in three spatial dimensions. Some general solutions to this equation are then given, before introducing methods for simulating acoustic fields from finite extent sources.

To derive the wave equation, we begin with the general equations of fluid dynamics. The conservation of mass in a fluid is a relation between density and particle velocity, and is described by

$$\frac{\partial \rho}{\partial t} + \nabla \rho \vec{v} \tag{3.1}$$

where ∇ is the Laplace operator

$$\nabla = \frac{\partial}{\partial x} + \frac{\partial}{\partial y} + \frac{\partial}{\partial z} \tag{3.2}$$

ρ is density and $\vec{v}$ is the velocity vector. For a non viscous fluid we have Euler's equation of motion

$$\rho \frac{\partial \vec{v}}{\partial t} = -\nabla \mathbf{p} \tag{3.3}$$

where $\mathbf{p}$ is pressure. Sound propagating through a fluid is disturbance and can be regarded as small amplitude perturbations from an ambient state. When no propagating sound is present, the fluid is described by the variables,
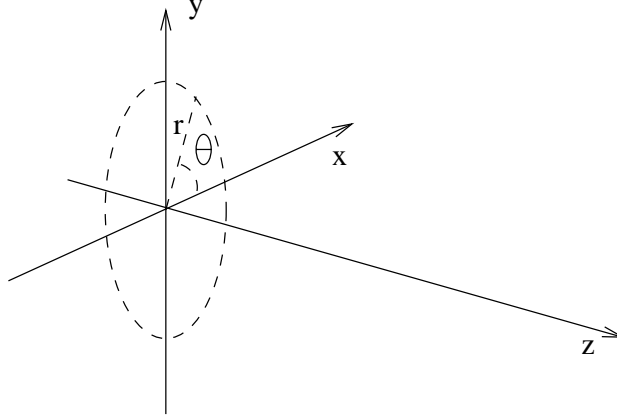
Figure 3.1: Coordinate system in Cartesian and cylindrical coordinates. z is the direction of propagation

$\vec{v}_0$, ρ_0 and $\mathbf{p}_0$, where $\vec{v}_0$ is initial velocity and ρ_0 and $\mathbf{p}_0$ is the ambient density and pressure. With propagating sound present, the fluid is described by

$$\mathbf{p} = \mathbf{p}_0 + \mathbf{p}', \quad \rho = \rho_0 + \rho', \quad \vec{v} = \vec{v}_0 + \vec{v}' \tag{3.4}$$

where the prime denotes small perturbations. In a homogeneous medium the initial velocity, $\vec{v}_0$, is zero. Assuming constant specific entropy, we have from the equation of state that $\mathbf{p}$ is a function of ρ, $\mathbf{p}(\rho)$, so a Taylor expansion of the acoustic pressure, $\mathbf{p}'$, can be written as

$$\mathbf{p}' = \left(\frac{\partial \mathbf{p}}{\partial \rho}\right)_0 \rho' + \frac{1}{2}\left(\frac{\partial^2 \mathbf{p}}{\partial \rho^2}\right)_0 (\rho')^2 + \dots \tag{3.5}$$

By using only the first term in the Taylor expansion, we get a linear approximation to (3.1) and (3.3)

$$\frac{\partial \rho'}{\partial t} + \rho_0 \nabla \vec{v}' = 0 \tag{3.6}$$

$$\rho_0 \frac{\partial \vec{v}'}{\partial t} = -\nabla \mathbf{p}' \tag{3.7}$$

If we let $c^2 = \left(\frac{\partial \mathbf{p}}{\partial \rho}\right)_0$, where c is the speed of sound, we have from (3.5)

$$\mathbf{p}' = c^2 \rho' \tag{3.8}$$

and

$$\frac{1}{c^2}\frac{\partial \mathbf{p}}{\partial t} + \rho_0 \nabla \vec{v}' = 0 \tag{3.9}$$

By taking the time derivative of (3.9), we get

$$\frac{1}{c^2}\frac{\partial^2 \mathbf{p}}{\partial t^2} + \rho_0 \nabla \left(\frac{\partial \vec{v}'}{\partial t} \right) = 0 \tag{3.10}$$

which from (3.7) is

$$\frac{1}{c^2}\frac{\partial^2 \mathbf{p}}{\partial t^2} + \nabla \nabla \mathbf{p}' = 0 \tag{3.11}$$

or

$$\nabla^2 \mathbf{p} - \frac{1}{c^2}\frac{\partial^2 \mathbf{p}'}{\partial t^2} = 0 \tag{3.12}$$

The last equation is the wave equation in three spatial dimensions and time, and is the basic equation for propagating waves. By replacing ∇ we get the more familiar form

$$\left(\frac{\partial^2}{\partial x^2} + \frac{\partial^2}{\partial y^2} + \frac{\partial^2}{\partial z^2} - \frac{\partial^2}{c^2 \partial t^2} \right) \mathbf{p} = 0 \tag{3.13}$$

We see that this equation is given in Cartesian coordinates, but it will also be presented in spherical and cylindrical coordinates.

3.2 Solutions of the wave equation

3.2.1 Cartesian coordinates

A general solution to (3.13) is derived by assuming a separable solution of the form [2]

$$s(x, y, z, t) = f(x)g(y)h(z)q(t) \tag{3.14}$$

By choosing each function on the right side as a complex exponential, we get

$$s(x, y, z, t) = Ae^{j(\omega t - k_x x - k_y y - k_z z)} \tag{3.15}$$

By putting s into (3.13), we get

$$k_x^2 s + k_y^2 s + k_z^2 s = \frac{\omega^2}{c^2} s \tag{3.16}$$

This means that s is a solution to (3.13) as long as the relation

$$k_x^2 + k_y^2 + k_z^2 = \frac{\omega^2}{c^2} \tag{3.17}$$

(a)   (b)
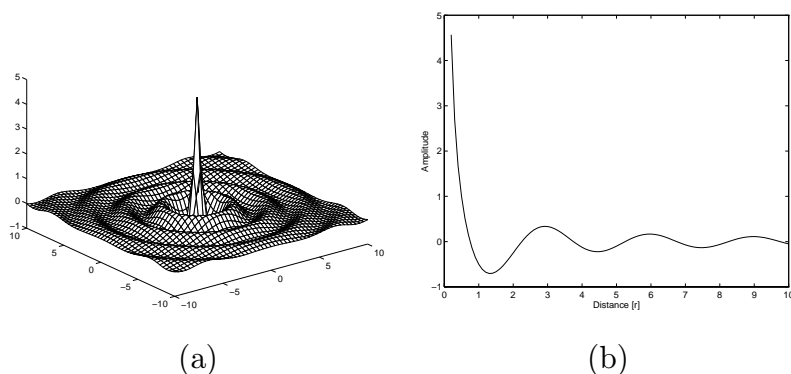
Figure 3.2: (a) Slice through the spherically symmetric solution of the wave equation (xy-plane through the origin). Z-axis is the amplitude. (b) Energy distribution along the radial distance, r, from the origin.

which is found by canceling s in (3.16), is satisfied. If as sensor is placed at $(x, y, z) = (0, 0, 0)$, the observed signal has the form of a complex exponential with frequency ω, given by

$$s(0, 0, 0, t) = Ae^{j\omega t} \tag{3.18}$$

The value of $s(x, y, z, t)$ at time $t = t_0$ is the same at all points in plane given by $k_x + k_y + k_z = C$, where C is a constant, so s represents a plane wave, meaning that the wavefronts of the propagating signal are planes perpendicular to the direction of propagation. To generate plane waves the source must have infinite extent so they are impossible to realize exactly, but from figure 2.1 in the previous chapter we have seen that the acoustic field far away from the source can be well approximated by plane waves.

3.2.2 Spherically symmetric solution

By introducing spherical coordinates, where

$$\begin{aligned}
r &= \sqrt{x^2 + y^2 + z^2} \\
\theta &= \tan^{-1}\left(\tfrac{y}{x}\right) \\
\phi &= \cos^{-1}\left(\tfrac{z}{r}\right)
\end{aligned} \tag{3.19}$$

the general wave equation in transformed coordinates can be found. But for our application a spherically symmetric solution is of interest. With spherical symmetry, the equation and solution are independent of both ϕ and θ. So for

spherically symmetric problems, the wave equation in spherical coordinates is given by

$$\frac{1}{r^2}\frac{\partial}{\partial r}\left(r^2\frac{\partial s}{\partial r}\right) = \frac{1}{c^2}\frac{\partial^2 p}{\partial t^2} \tag{3.20}$$

and a solution is given by

$$s(r,t) = \frac{A}{r}e^{j(\omega t - kr)} \tag{3.21}$$

This solution represents a wave propagating outward from the origin in all directions, with wavefronts as spheres in space as shown in figure 3.2 (a), where the energy in a slice through the spherical distribution is shown. The $1/r$ factor means that the energy is dampened along a line from the origin as shown in figure 3.2 (b), which is natural since the energy is distributed in increasing spheres as r becomes larger. The solution can be thought of as representing an antenna, radiating energy in all directions. This solution plays an important role in Huygen's principle which will be presented next.

3.3   Simulation of acoustic fields

3.3.1   Huygen's principle

The acoustic field generated by a vibrating piston transducer, is similar to
the field of a plane wave traveling through a hole in the wall as described in
the previous chapter. The wave does not propagate in a straight line, but
diffracts in all directions as shown in figure 2.3. The amount of diffraction
depends on the wavelength and the size of the hole, or in our case, the size
of the transducer. Diffraction theory began when Christian Huygen in the
late seventeenth century tried to explain why shadow edges were not sharp.
His theory was that each point on a traveling wavefront could be considered
a source of spherical radiation, and that the wavefront at a later time was a
sum of these spherical radiating sources. This is known as Huygen's princi-
ple. This principle gives an intuitive feeling of why a larger diameter of the
transducer gives a narrower beam. If we had an infinitely small transducer,
just a point in space, it would be a source of one spherical wave, radiating
energy in all directions described by the spherically symmetric solution in
the previous section. With a larger transducer, the center of the beam is a
sum of many spherical waves. At the edges, the waves from the other side
of the transducer has lost energy due to spherical propagation, which gives
less energy compared to the center. An alternative to a larger diameter is to
increase the frequency of the transducer. This gives a smaller wavelength,
and therefore a larger diameter measured in wavelengths.

3.3.2   Rayleigh-Sommerfeld diffraction formula

Huygen's principle has later been given a mathematical foundation, resulting
in the Rayleigh-Sommerfeld diffraction formula which predicts the acoustic
field generated from a finite aperture. The formula, which predicts the ve-
locity potential or pressure field, is given by [2]

$$s(\vec{r_0}) = \frac{1}{j\lambda} \int \int_A s(\vec{r_1}) \frac{e^{jkr_{01}}}{r_{01}} \cos\phi dA \qquad (3.22)$$

where $s(\vec{r_0})$ is the field at point $\vec{r_0}(x_0, y_0, z)$ in space, $\vec{r_1}(x_1, y_1, 0)$ is a point
on the transducer, $s(\vec{r_1})$ is the field at the transducer at point r_1, r_{01} is the
distance between $\vec{r_1}$ and $\vec{r_0}$, ϕ is the angle between a vector normal to the
transducer and the vector $\vec{r_0} - \vec{r_1}$, and A is the aperture. The field at point
$\vec{r_0}$ is a sum of spherical waves from infinitesimal points on the transducer,
so we see the relation with Huygen's principle. To simulate the acoustic
field generated by a transducer with continuous wave excitation, (3.22) is
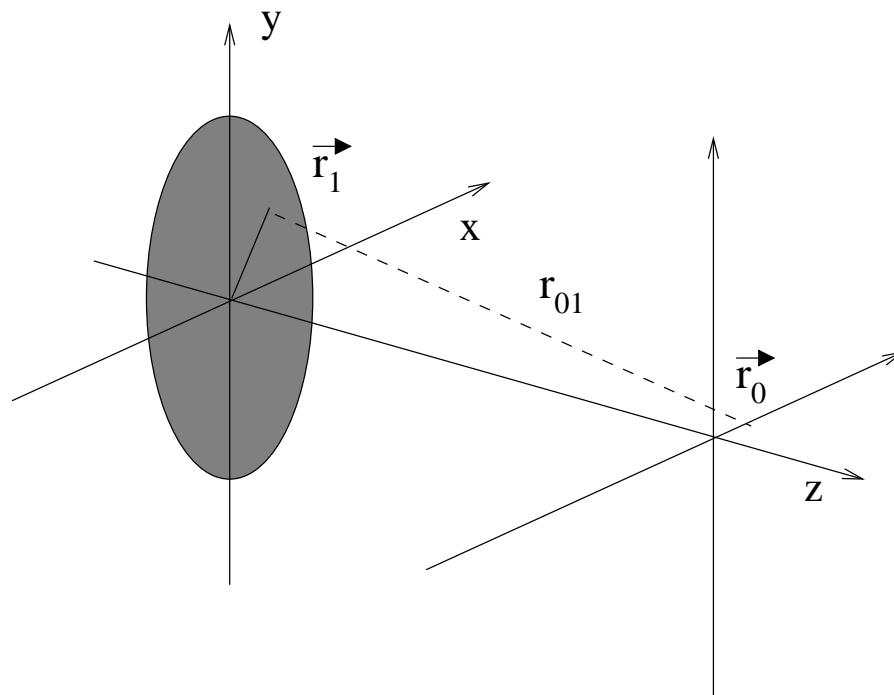
Figure 3.3: Coordinate system for the Rayleigh-Sommerfeld diffraction formula. $\vec{r_0}$ is the point where you want to calculate the acoustic pressure, $\vec{r_1}$ is a point on the transducer surface and r_{01} is the distance between $\vec{r_0}$ and $\vec{r_1}$.

evaluated at the points where you want to predict the field. The term $s(\vec{r_1})$ could be used to include aperture weights, for example when simulating fields from an annular array transducer.

For simulation of multiple frequency waves, like pulses used in pulse-echo imaging, the temporal frequency version of the Rayleigh-Sommerfeld formula could be used. If the aperture is a disc with radius a, this formula is given by [3]

$$
\begin{aligned}
\mathbf{S}(\vec{r_0}, \omega) \ \ &= \tfrac{1}{j\lambda} \int_0^a \int_{-\pi}^{\pi} \mathbf{S}(\vec{r_1}, \omega) e^{ikr_{01}} \tfrac{z}{r_{01}^2} r_1 dr_1 d\theta_1 \\
&+ \tfrac{1}{2\pi} \int_0^a \int_{-\pi}^{\pi} \mathbf{S}(\vec{r_1}, \omega) e^{ikr_{01}} \tfrac{z}{r_{01}^3} r_1 dr_1 d\theta_1
\end{aligned}
\tag{3.23}
$$

where $\mathbf{S}(\vec{r_0}, \omega)$ is the temporal frequency of the field at point $\vec{r_0}(x_0, y_0, z)$, $\mathbf{S}(\vec{r_1}, \omega)$ is the temporal frequency at the surface of the transducer at point $\vec{r_1}(x_1, y_1, 0)$, $r_1 = \sqrt{x_1^2 + y_1^2}$ and $\theta_1 = \tan^{-1}(y_1/x_1)$, see figure 3.3. Simulation is now done by finding the frequency weighting at the surface of the transducer, evaluate (3.23) at all desired spatial points, and then doing the inverse temporal Fourier transform of the resulting field, $\mathbf{S}(\vec{x_0}, \omega)$. A second term has been included in (3.23) to give better predictions very close to the transducer. Note that this term can be neglected when $r \gg \lambda/2\pi$. The obliquity factor, $\cos\phi$ which is approximately one, has been omitted. Both (3.22) and (3.23) involves double integrals, and are very time-consuming to evaluate. Effort has been made to simplify the expressions by doing some approximations. Two classical approximations are the Fresnel and the Fraunhofer approximations. The first gives the idea of a simulation algorithm based on the fast Fourier transform, the second gives further intuition of the relationship between diffraction and aperture size.

The Fresnel approximation is based on the assumption that the term $\cos\phi$ in (3.22) is approximately one, and that r_{01} is approximately equal to the distance d between the aperture plane and a parallel observation plane containing the observation point $\vec{r_0}$. This approximation then becomes

$$
s(x, y, d) = \frac{e^{jkd}}{j\lambda d} \int \int_A s(\hat{x}, \hat{y}) e^{\frac{jk[(x-\hat{x})^2 + (y-\hat{y})^2]}{2d}} d\hat{x} d\hat{y}
\tag{3.24}
$$

where the coordinates $(\hat{x}, \hat{y})$ are points on the transducer. This equation is a two-dimensional convolution between the aperture function $s(\hat{x}, \hat{y})$ and

$$
h(x, y, d) = \frac{e^{jkd}}{j\lambda d} e^{\frac{jk(x^2 + y^2)}{2d}}
\tag{3.25}
$$

Note that a spatial convolution with discrete values could be evaluated by a two-dimensional fast Fourier transform.

The second approximation, the Fraunhofer approximation, takes the Fresnel approximation a step further and applies when the observation plane is far away from the aperture. By expanding the quadratic phase term in (3.24) and assuming $d \gg D^2\lambda$, where D is the dimension of the transducer, the quadratic phase factor, $e^{\frac{jk(\hat{x}^2+\hat{y}^2)}{2d}} \approx 1$, can be neglected. This results in the approximation

$$s(x,y) = \frac{e^{jkd}}{j\lambda d}e^{\frac{jk(x^2+y^2)}{2d}} \int\int_A s(\hat{x},\hat{y})e^{\frac{jk(x\hat{x}+y\hat{y})}{d}}\,d\hat{x}d\hat{y} \qquad (3.26)$$

which can be interpreted as a two-dimensional Fourier transform of $s(\hat{x},\hat{y})$. Based on temporal Fourier transform theory, we know that a short signal in time is broad in frequency, which is the same for spatial transforms. This again implies that a large transducer generates a narrow beam.

3.3.3 Simulation of acoustic fields using the FFT

The convolution present in the Fresnel approximation, implies that evaluating the discrete version of the continuous field in (3.22), could be done using a two-dimensional fast Fourier transform. Williams *et. al* [4] use the FFT in a similar way to evaluate the Rayleigh integral which predicts the acoustic pressure in space,

$$p(x,y,z) = -j\omega\rho \int_{-\infty}^{\infty} \int_{-\infty}^{\infty} \hat{p}(\hat{x},\hat{y})\frac{e^{jkR}}{2\pi R}\,d\hat{x}d\hat{y} \qquad (3.27)$$

where

$$R = (x - \hat{x})^2 + (y - \hat{y})^2 + z^2 \qquad (3.28)$$

and ρ is density. This formula is a scaled version of (3.22) without the obliquity factor $\cos\phi$. (3.27) can be written as a convolution

$$p(x,y,d) = \hat{p}(x,y) * h(x,y,d) \qquad (3.29)$$

where

$$h(x,y,d) = -\frac{j\omega\rho}{2\pi}\frac{e^{jk\sqrt{(x^2+y^2+d^2)}}}{\sqrt{x^2+y^2+d^2}} \qquad (3.30)$$

for $d = z$. By applying that convolution in space gives multiplication in wavenumber, (3.27) could be evaluated by the expression

$$p(x,y,d) = \mathcal{F}^{-1}\left\{\hat{P}(k_x,k_y)H(k_x,k_y,d)\right\} \qquad (3.31)$$

where $\mathcal{F}^{-1}$ denotes the inverse two-dimensional Fourier transform and $\hat{P}(k_x, k_y)$ and $\hat{H}(k_x, k_y, d)$ are the Fourier transforms of $\hat{p}(x, y)$ and $h(x, y, d)$. The algorithm for computing $p(x, y, d)$ using the FFT is then

1. Calculate the discrete Fourier transform of $\hat{p}(x, y)$ using the FFT and call it $\hat{P}_D$

2. Calculate the analytic form of $H(k_x, k_y, d)$

3. Multiply results 1. and 2. $P_D = \hat{P}_D H$

4. Calculate the inverse discrete Fourier transform of the result in 3. That gives $p = \mathcal{F}_D^{-1}\left\{\hat{P}_D H\right\}$ where $\mathcal{F}_D^{-1}$ denotes inverse discrete Fourier transform.

With a large number of samples, even evaluation of the two-dimensional FFT can be very time consuming. This thesis only considers circular symmetric beams which is the case for the zeroth order Bessel beam and X wave. Exploiting this circular symmetry leads us to the Hankel transform and its discrete version.

3.3.4   Hankel transform

The two-dimensional Fourier transform is given by

$$G(k_x, k_y) = \int_{-\infty}^{\infty} \int_{-\infty}^{\infty} g(x, y)e^{-j2\pi(k_x x + k_y y)}dxdy \tag{3.32}$$

In polar coordinates, where

$$
\begin{aligned}
r &= \sqrt{x^2 + y^2} \\
\theta &= \tan^{-1}\left(\tfrac{y}{x}\right) \\
R &= \sqrt{k_x^2 + k_y^2} \\
\phi &= \tan^{-1}\left(\tfrac{k_y}{k_x}\right)
\end{aligned}
\tag{3.33}
$$

(3.32) becomes

$$G(R, \phi) = \int_0^{\infty} \int_0^{2\pi} g(r, \theta)e^{-j2\pi rR(\cos\theta\cos\phi + \sin\theta\sin\phi)}rd\theta dr \tag{3.34}$$

If $g(r, \theta)$ is circular symmetric, meaning that the function is independent of θ, then

$$g(r, \theta) = g_R(r) \tag{3.35}$$

and (3.34) can be written as

$$G(R, \phi) = \int_0^\infty g_R(r) \int_0^{2\pi} e^{-j2\pi rR(\cos\theta\cos\phi + \sin\theta\sin\phi)} rd\theta dr \qquad (3.36)$$

$$= \int_0^\infty g_R(r) \int_0^{2\pi} e^{-j2\pi rR\cos(\theta-\phi)} rd\theta dr \qquad (3.37)$$

With the Bessel function identity [5]

$$J_0(x) = \frac{1}{2\pi} \int_0^{2\pi} e^{-jx\cos(\theta-\phi)} d\theta \qquad (3.38)$$

inserted into (3.37), the dependence on ϕ disappears and the expression can be simplified to

$$G(R) = 2\pi \int_0^\infty g_R(r) J_0(2\pi rR) dr \qquad (3.39)$$

$G(R)$ is now a circular symmetric two-dimensional Fourier transform of a circular symmetric function, and is referred to as the Hankel transform of zeroth order, Fourier-Bessel transform or rotational Fourier transform. The two integrals in (3.32) are reduced to one, so algorithms simulating acoustic fields generated by circular symmetric sources can take advantage of this to reduce computational time. What is important is that the convolution property,

$$g(x, y) * h(x, y) = \mathcal{F}^{-1} \{G(k_x, k_y) H(k_x, k_y)\} \qquad (3.40)$$

is still valid for the Hankel transform, so a similar simulation method like the one based on the FFT described in the previous section, can be used. This requires a discrete version of the Hankel transform which will be introduced in the next section.

3.3.5 A method for computing a discrete Hankel transform

The Hankel transform of general order or generalized Fourier-Bessel transform is given by the transform pair [6]

$$F_\nu(R) = \int_0^\infty f(x) J_\nu(xR) x dx, \quad \nu \geq -\tfrac{1}{2} \qquad (3.41)$$

and

$$f(x) = \int_0^\infty F_\nu(R) J_\nu(xR) R dR, \quad \nu \geq -\tfrac{1}{2} \qquad (3.42)$$

To determine a discrete version of the Hankel transform, the assumption
$f(x) = 0$ for all $x > T$ is made. By defining

$$r = \frac{RT}{j_N} \tag{3.43}$$

where j_N is the Nth zero of the Bessel function, $J_\nu(x)$, the forward transform
can be written as [6]

$$F_\nu(rj_N/T) = T^2 \int_0^1 f(xT) J_\nu(xrj_N) r\, dr \tag{3.44}$$

and the inverse transform as

$$f(xT) = \frac{j_N^2}{T^2} \int_0^\infty F_\nu(rj_N/T) J_\nu(xrj_N) r\, dr \tag{3.45}$$

By using Lommel's generalized version of the Fourier-Bessel series, $f(xT)$
can be written as

$$f(xT) = \begin{cases} \sum_{m=1}^\infty \frac{2C_m}{J_{\nu+1}^2(j_m)} J_\nu(j_m x), & 0 \le x \le 1 \\ 0, & 1 < x \le \infty \end{cases} \tag{3.46}$$

where j_m are the zeros of $J_\nu(x)$ sorted in ascending order, and the coefficients
C_m are given by

$$C_m = \int_0^1 x f(xT) J_\nu(j_m x)\, dx \tag{3.47}$$

Assuming $C_m = 0$ for all $m \ge N$, we have from (3.44) that

$$F_\nu(j_m/T) = T^2 C_m \tag{3.48}$$

when $r = \frac{j_m}{j_N}$ and by applying this to (3.46) we get the relation

$$f(xT) = \begin{cases} \sum_{m=1}^{N-1} \frac{2F_\nu(j_m/T)}{J_{\nu+1}^2(j_m)T^2} J_\nu(j_m x), & 0 \le x \le 1 \\ 0, & 1 \le x \le \infty \end{cases} \tag{3.49}$$

This last expression gives a relationship between $f(xT)$ and its Hankel trans-
form at certain values of r. To find a similar relationship between $F(rj_N/T)$
and $f(xT)$ the orthogonality relation [6]

$$\frac{4}{J_{\nu+1}^2(j_m)j_N^2} \sum_{p=1}^{N-1} \frac{J_\nu(j_m j_p/j_N) J_\nu(j_i j_p/j_N)}{J_{\nu+1}^2(j_p)} = \delta_{m,i}, \quad m,i < N \tag{3.50}$$

is used. If we set $x = j_p/j_N$ in (3.49) and multiply both sides by $J_\nu(j_p j_i/j_N)$ and sum, we get

$$F_\nu(j_i/T) = \frac{T^2}{j_N^2} \sum_{p=1}^{N-1} \frac{2J_v(j_p j_i/j_N)}{J_\nu^2(j_p)} f(j_p T/j_N) \tag{3.51}$$

The exact discrete Hankel transform pair is then

$$f(i) = \frac{1}{T^2} \sum_{m=1}^{N-1} Y_\nu(m,i) F_\nu(m) \tag{3.52}$$

$$F_\nu(m) = \frac{T^2}{j_N^2} \sum_{i=1}^{N-1} Y_\nu(m,i) f(i) \tag{3.53}$$

where

$$f(i) = f(j_i T/j_N) \tag{3.54}$$
$$F_\nu(m) = F_\nu(j_m/T) \tag{3.55}$$

and $Y_\nu(i,m)$ is given by

$$Y_\nu(i,m) = 2\frac{J_\nu(j_i j_m/j_N)}{J_{\nu+1}^2(j_m)} \tag{3.56}$$

3.3.6 Simulation of acoustic fields using the DHT

The methods now presented for simulating acoustic fields from a circular source is based on the discrete Hankel transform in the previous section. They use a zeroth order Hankel transform which means setting $\nu = 0$ in the transform pair. While the described Hankel transform gives output in the Fourier domain in radians per unit length, Christopher *et. al*[7] have converted the output to cycles per unit length. The transform pair is then given by

$$f(i) = \frac{1}{2\pi T^2} \sum_{m=1}^{N-1} Y(m,i) F_\nu(m) \tag{3.57}$$

$$F(m) = \frac{2\pi T^2}{j_N^2} \sum_{i=1}^{N-1} Y(m,i) f(i) \tag{3.58}$$

where $Y(i,m)$ is given by

$$Y(i,m) = 2\frac{J_0(j_i j_m/j_N)}{J_1^2(j_m)} \tag{3.59}$$

The subscript ν which is zero, has here been dropped. To implement the discrete Hankel transform, the zeros of the Bessel-function, $J_0(x)$, must be found. The implementation done in this thesis uses a quasi-Newton method to find these zeros. In addition, a table with the $Y(i, m)$-values must be calculated. This table can be very time consuming to generate if a large number of samples is required, but can be stored and reused if simulations are done with the same number of samples. Note that the input and output values of the transforms are not equidistant samples as is for the fast Fourier transform. This must be taken into consideration when plotting the results.

The analytical expression of the response function used to calculate the normal velocity field in a plane, z_1, due to pressure from a source plane, z_0, is [7]

$$h_v(z, r) = -\frac{1}{2\pi}\frac{z}{d^2}\left(j2\pi\frac{f}{c} - \frac{1}{d}\right)e^{jkd} \qquad (3.60)$$

where

$$z = z_1 - z_0, \quad d = \sqrt{r^2 + z^2} \qquad (3.61)$$

Convolving this expression with the normal velocity point source in the plane, z_0, gives the normal velocity field in the plane, z_1. The analytical Hankel transform of this expression is

$$H(z, R) = \begin{cases} e^{j2\pi z\sqrt{(f/c)^2 - R^2}}, & |R| \le f/c \\ e^{-2\pi z\sqrt{R^2 - (f/c)^2}}, & |R| \ge f/c \end{cases} \qquad (3.62)$$

To apply the discrete Hankel transform to propagation of fields, lateral sampling of the source function, $s(r)$, and propagation function must be done for some finite extent of the aperture. The sampled field must be larger than the source radius. The DHT-algorithm is similar to the FFT-based algorithm in section 3.3.3, and is based on the fact that convolution in the spatial domain corresponds to multiplication in the transform domain. Two different algorithms, one sampling the propagation function (3.60), and the other sampling its transform function (3.62), will now be presented. Note that because of the circular symmetry of the Hankel transform, only circular symmetric sources can be used with these algorithms.

The first approach, sampling $h_v(z, r)$, is referred to as spatially sampled convolution (SSC), and is as follows:

1. Select a radius, r_d, greater than the source radius, a. This determines the transform extent as $T \ge r_d + a$.

2. Select a spatial sampling rate, ψ, which exceeds the Nyquist rate. Christopher *et. al*[7] proposes $4 \times f/c$ to ensure finely sampled output. The number of lateral samples is then $N = \psi \times T$.

3. Sample the source function, $s(r)$, and call the resulting collection of samples $s_d(i)$, $i = 1, .., N$. Compute the DHT of these values and call the complex transform output $S_d(m)$, $m = 1, .., N$.

4. Sample $h(z, r)$, where z is the propagation distance from the source, and call the samples $h_d(i)$, $i = 1, ..N$. Compute the DHT of these values and call the complex transform output $H_d(m)$, $m = 1, ..N$.

5. Compute the product $S_d(m) \times H_d(m)$, $m = 1, .., M$, and do the inverse DHT of this product to obtain the field result, $u_d(z, i)$, $i = 1, ..N$.

The u_d values are now samples of the normal velocity field at distance, z, so the algorithm has performed discrete convolution between the source and propagation function. The normal velocity field can be converted to acoustic pressure by the impedance relation

$$p = \rho c u \tag{3.63}$$

where p is pressure, ρ is density and u is the normal velocity. A second approach, referred to as frequency sampled convolution (FSC), samples the analytic transform of $h_v(z, r)$, and only differs in step four of the SSC-algorithm:

4. Directly sample $H(z, R)$ to obtain $\hat{H}_d(m)$, $m = 1, ..N$. Use these values as the H_d values in the SSC-algorithm.

Although the analytical analogs of these two approaches are equivalent, the finite extent sampling introduces significant differences. Both algorithms will be used in this thesis. The SSC-algorithm will be used in linear single step simulation, and a modified version of the FSC-algorithm will be used in a multi-step simulation under nonlinear conditions.

Christopher *et. al*[7] have simulated a 3 MHz, unfocused piston transducer with 10 mm radius. The medium is water with speed of sound $c = 1500$ m/s, and no attenuation is included. The transform extent is $T = 4$ cm, and sampling the field at $4 \times f/c$ gives a sampling rate of 80 samples/cm, and a total number of samples, $N = 320$. Fig. 3.4 (a) and (b) shows the output from the two algorithms at $z = 0.05$ cm, while fig. 3.4 (c) and (d) shows the output at $z = 20$ cm. Note the miserable result from the FSC-algorithm at $z = 20$ cm, caused by the direct sampling of the infinite extent transform function. This algorithm can be greatly improved by applying a ray theory truncation of the analytical Hankel transform of $h_v(z, r)$.

(a)

(b)

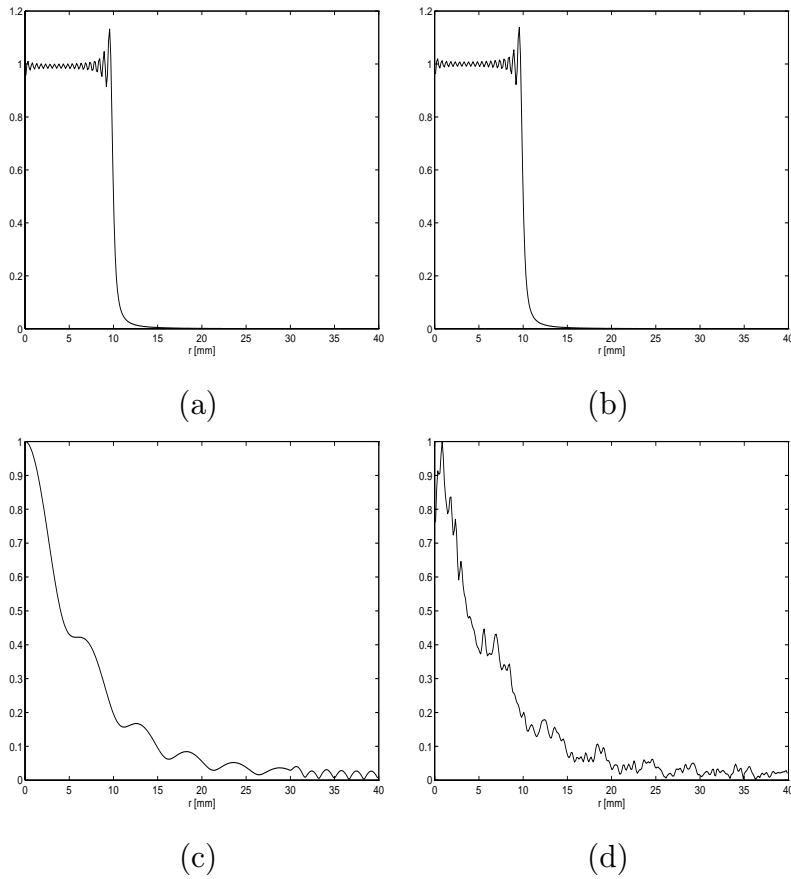(c)

(d)

Figure 3.4: Normal velocity field simulation from an unfocused piston trans-
ducer of radius 1 cm. The number of samples, $N = 320$, and the spatial
extent $T = 4$ cm. (a) Simulation using the SSC-algorithm at $z = 0.05$ cm
(b) Corresponding simulation using the FSC-algorithm (c) SSC at $z = 20$ cm
(d) FSC at $z = 20$ cm. Note the miserable result from the FSC-algorithm at
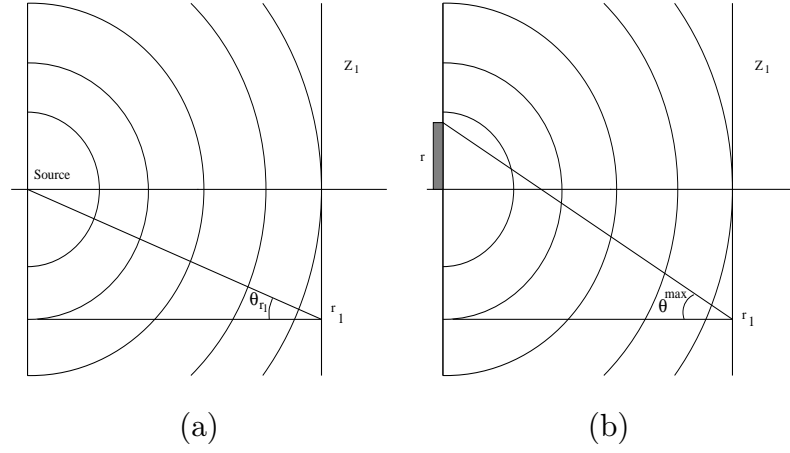$z = 20$ cm.

(a)   (b)

Figure 3.5: Geometry for the truncation of the FSC-algorithm (a) At the point, r_1, the lateral frequency from a spherical wave is $\eta = (f/c)\sin(\theta_{r_1})$. (b) Combining ray theory with Huygen's principle gives maximum lateral frequency $\eta_{max} = (f/c)\sin(\theta^{max})$

Ray theory suggests that the lateral spatial frequency, η_{r_i}, of the field in the plane z_1 at point (r_i, z) is given by [7]

$$\eta_{r_i} = (f/c)\sin\theta_{r_i}, \quad \text{cycles/unit length} \tag{3.64}$$

where θ_{r_1} is the angle given by the geometry in figure 3.5. Equation (3.64), combined with Huygen's principle, can be used to find a reduced sampling rate. From Huygen's principle we know that each point on the transducer is a source of a spherical wave. From the geometry in figure 3.5 (b), the most distant source contributing to the field at point (r_1, z), has the maximum angle, θ_1^{max}. From (3.64), the maximum lateral spatial frequency at point (r_1, z), is given by

$$\eta_{max} = (f/c)\sin\theta^{max} \tag{3.65}$$

This expression can now be used to find a reduced minimum sampling rate. The new sampling rate can be applied to the SSC-algorithm by computing fewer samples of $h_v(z, r)$, or to the FSC by truncating $H(z, R)$ so the maximum frequency is given by (3.65). This means setting $H(z, R) = 0$ when $R > \eta_{max}$. The truncated FSC-algorithm is referred to as the ray theory-updated FSC-algorithm (RFSC).

Consider again the piston transducer example described previously. Obtaining good field results out to a lateral distance, r_d, of 5 cm at $z = 20$ cm,
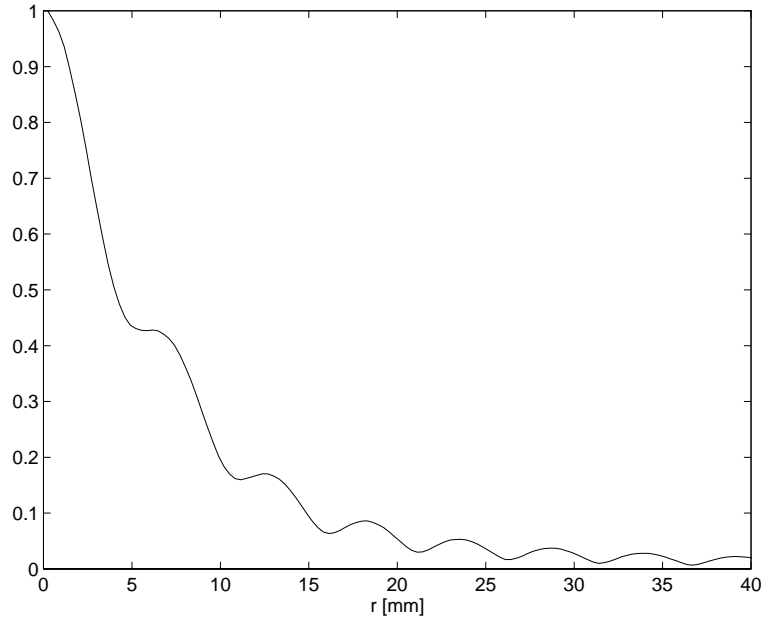
Figure 3.6: Normal velocity field for unfocused piston source at $z = 20$ cm, calculated by the RFSC-algorithm.

gives the maximum lateral spatial frequency

$$\eta_{max} = (f/c)\sin(\theta_{r_d}) \tag{3.66}$$

where

$$\theta_{r_d} = \tan^{-1}\left(\frac{r_d + a}{z}\right) = 16.69° \tag{3.67}$$

and $a = 1$ cm is the transducers radius. By choosing $T = 10$ cm, the minimum number of samples is $N = 115$. Figure 3.6 shows the RFSC-algorithm output from this example. It is only shown out to $r = 4$ cm.

Chapter 4

Theory of limited diffraction beams

While spherically focused beams have an optimal area of focus, the sidelobes grow and the beam gets broader when moving in either direction away from the focusing point. The motivation for transmission of limited diffraction beams, is that they have an approximately depth-independent lateral beam-profile, so focusing is the same in every plane normal to the direction of propagation within the depth of field. The exact expressions for the limited diffraction beams are in fact nondiffracting, meaning that the have exactly the same lateral field distribution, even when traveling to infinity. But the theoretical beams require infinite aperture and bandwidth, practical beams are only approximately nondiffracting for a finite distance, so they have been termed limited diffraction beams.

4.1 General limited diffraction solution to the wave equation

The wave equation in cylindrical coordinates is given by

$$\left[\frac{1}{r} \frac{\partial}{\partial r} \left(r \frac{\partial}{\partial r} \right) + \frac{1}{r^2} \frac{\partial^2}{\partial \theta^2} + \frac{\partial^2}{\partial z^2} - \frac{1}{c^2} \frac{\partial^2}{\partial t^2} \right] \mathbf{p} = 0 \tag{4.1}$$

where $r = \sqrt{x^2 + y^2}$ and θ is the azimuth angle. The solution, $\mathbf{p}$, represents acoustic pressure of the wave at the spatial coordinates r, θ and z, at time t. A general solution to this equation, given by Lu *et. al* [8], is

$$\mathbf{p}(s) = \int_0^\infty T(k) \left[\frac{1}{2\pi} \int_{-\pi}^{\pi} A(\xi) f(s) d\xi \right] dk \tag{4.2}$$

where

$$s = \alpha_0(k,\zeta)r\cos\left(\theta - \xi\right) + b(k,\zeta)\left[z \pm c_1(k,\zeta)t\right] \tag{4.3}$$

and

$$c_1(k,\zeta) = c\sqrt{1 + \left[\alpha_0(k,\zeta)/b(k,\zeta)\right]^2} \tag{4.4}$$

where $T(k)$, $A(\xi)$ and $f(s)$ are well behaved complex functions. If $c_1(k,\zeta)$ is independent of k, (4.2) represents a family of nondiffracting beams. Before introducing the Bessel beam and X wave, we will first take a look at another nondiffracting solution of (4.1), the Axicon beam.

4.2   Axicon beam

The Axicon beam is produced from a conical transducer, where the conical transducer is defined by the Axicon angle ζ, see figure 4.1. This is the angle between the cone and a transverse plane, where $\zeta = 0$ is equivalent to a flat transducer. From the shape of the transducer, we see that it is focusing on a line along the z-axis, as opposed to a spherically focused transducer, which focuses on a point. The line of focus extends to where the lines perpendicular to the cone edges crosses, which means that the depth of focus is dependent on the size of the transducer and the Axicon angle, and can be shown from geometry to be [9]

$$\text{DOF}_A = \frac{R}{\tan\zeta} \tag{4.5}$$

where R is the radius of the transducer.

An approximation to the exact acoustic field generated by this transducer is given by

$$\mathbf{p}_{A_0} = J_0\left(kr\sin\zeta\right)e^{i(kz\cos\zeta - \omega t)} \tag{4.6}$$

This is the zeroth order Axicon beam, the nth-order is given by

$$\mathbf{p}_{A_n} = J_n\left(kr\sin\zeta\right)e^{i(kz\cos\zeta - \omega t + n\theta)} \tag{4.7}$$

To show that this is a solution of the wave equation, we can insert $\mathbf{p}_{A_n}$ into the left side of (4.1), and verify that it becomes zero. Another way is to show that (4.7) fits in the solution given by (4.2). If in equation (4.2) we let $T(k) = \delta(k - k')$, where $k' = \frac{\omega}{c}$, $f(s) = e^s$, $A(\xi) = i^n e^{in\xi}$, $\alpha_0(k,\zeta) = -ik\sin\zeta$, $b(k,\zeta) = ik\cos\zeta$, we get

$$s = -ik\sin(\zeta)r\cos(\theta - \xi) + ik\cos\zeta\left[z + c_1(k,\zeta)t\right] \tag{4.8}$$
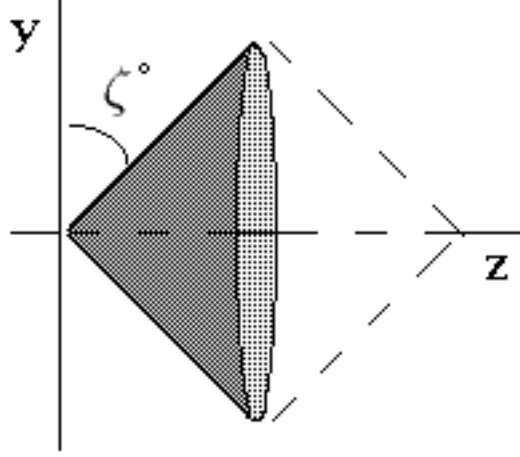
Figure 4.1: Example of a conical transducer used to produce an Axicon beam. The depth of field extends to where the lines perpendicular to the cone edges crosses, and is dependent on the angle, ζ.

and

$$c_1(k, \zeta) = c \sqrt{1 + \left(\frac{-ik \sin \zeta}{ik \cos \zeta} \right)^2} = \frac{c}{\cos \zeta} \tag{4.9}$$

Inserting this into (4.2), gives

$$\mathbf{p_{A_n}}(s) = \frac{1}{2\pi} \int_{-\pi}^{\pi} i^{-n} e^{in(\theta-\xi)} e^{-i\frac{\omega}{c}(\sin\zeta r \cos(\theta-\xi) - [z \cos\zeta + ct])} e^{in\theta} d\xi \tag{4.10}$$

$$= \left[\frac{1}{2\pi} \int_{-\pi}^{pi} i^{-n} e^{in(\theta-\xi)} e^{-i\frac{\omega}{c}\sin\zeta r \cos(\theta-\xi)} d\xi \right] e^{i(\frac{\omega}{c} z \cos\zeta - \omega t + n\theta)} \tag{4.11}$$

$$= J_n \left(\frac{\omega}{c} r \sin\zeta \right) e^{i(\frac{\omega}{c} z \cos\zeta - \omega t + n\theta)} \tag{4.12}$$

which is the same as (4.7). From (4.9), we see that $c_1(k, \zeta)$ is independent of k, which means that if a broadband pulse is excited from an Axicon transducer, all frequency components in the generated beam will have the same speed, so the beam will be nondispersive.

4.3   Bessel beam

The nth order Bessel beam is given by [10]

$$\mathbf{p_{B_n}} = J_n(\alpha r) e^{i(\beta z - \omega t + n\theta)} \tag{4.13}$$

for integer values of n, where

$$\alpha^2 + \beta^2 = \left(\frac{\omega}{c}\right)^2 \tag{4.14}$$

If we set $T(k) = \delta(k - k')$ where $\delta(k - k')$ is the delta function, $k' = \frac{\omega}{c}$, $A(\xi) = i^n e^{in\xi}$, $f(s) = e^s$, $\alpha_0(k, \zeta) = -i\alpha$ and $b(k, \zeta) = i\beta$, (4.4) becomes

$$
\begin{aligned}
c_1(k, \zeta) &= c\sqrt{1 + [-i\alpha/i\beta]^2} \\
&= c\sqrt{\frac{(\alpha+\beta)^2}{\beta^2}} \\
&= \frac{\omega}{\beta}
\end{aligned}
\tag{4.15}
$$

In the last transition relation (4.14) is used. Inserting this into (4.3) gives

$$s = -i\alpha r \cos(\theta - \xi) + i\beta \left[z - \frac{\omega}{\beta}\right]t \tag{4.16}$$

Inserting all this into (4.2) gives

$$
\begin{aligned}
\mathbf{p}_{B_n} &= \int_0^\infty \delta(k - k')\left[\frac{1}{2\pi}\int_{-\pi}^{\pi} i^n e^{in\xi} e^{-i\alpha r \cos(\theta-\xi)+i\beta z - ikct}d\xi\right]dk & (4.17) \\
&= \frac{1}{2\pi}\int_{-\pi}^{\pi} i^n e^{in\xi} e^{-i\alpha r \cos(\theta-\xi)+i\beta z - i\omega t}d\xi & (4.18) \\
&= \left[\frac{1}{2\pi}\int_{-\pi}^{\pi} i^n e^{in\xi} e^{-in\theta} e^{-i\alpha r \cos(\theta-\xi)}\right]e^{i\beta z - i\omega t}e^{in\theta}d\xi & (4.19) \\
&= \left[\frac{1}{2\pi}\int_{-\pi}^{\pi} i^{-n} e^{in(\theta-\xi)} e^{i\alpha r \cos(\theta-\xi)}\right]e^{i\beta z - i\omega t + in\theta}d\xi & (4.20) \\
&= J_n(\alpha r)e^{i(\beta z - \omega t + n\theta)} & (4.21)
\end{aligned}
$$

We have that speed $c_1(k, \zeta) = \frac{\omega}{\beta} = k'\beta c$, which means that $c_1(k, \zeta)$ is dependent on k'. So in this case, if $T(k)$ is a function containing more than one frequency, $c_1(k, \zeta)$ would be different for each k, and (4.13) would represent a dispersive wave.

If $n = 0$, (4.13) is a plane wave weighted by a Bessel-function for different radial distances, r. The zeroth order Bessel beam is then a superposition of plane waves traveling at angle ϕ, where ϕ is given by [9]

$$\phi = \sin^{-1}(\alpha\lambda/2\pi) \tag{4.22}$$

and λ is the wavelength. ϕ can be interpreted as the Axicon angle, ζ, for the Axicon beam so the Bessel beam has a similar conical focus. But unlike the
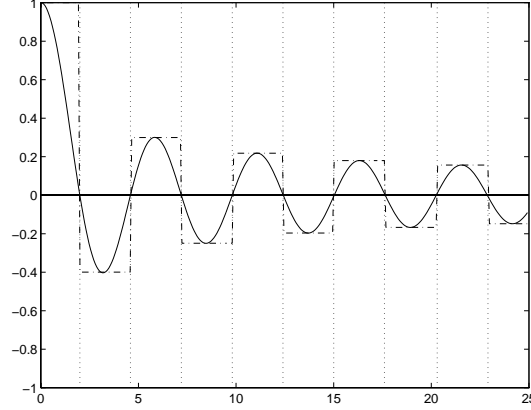
Figure 4.2: The $J_0(\alpha r)$-function in (4.13) with $\alpha = 1202$ m^{-1}, together with a possible discrete version of it. The dotted lines are the division of the elements in a 10 element 50 mm annular array. Elements are cut on the zeros of the Bessel function, $J_0(\alpha r)$. The discrete function inside the boundaries of each element is used as weight for that particular element.

Axicon angle, ϕ is dependent on the transmitted frequency. This is why the Bessel beam is dispersive as seen from the expression of propagation speed, c_1. As an analog to the Axicon transducer, exciting a broadband Bessel beam could be compared to having a different angle of the cone for each transmitted frequency.

Since the zeroth order Bessel beam is simply a weighted plane wave, it could be implemented on an annular array transducer, weighting each ring with the value of $J_0(\alpha r_n)$, where r_n is within the boundaries of ring n. Each ring could be cut on the zero-crossings of $J_0(\alpha r)$ [11]. Figure 4.2 shows the $J_0(\alpha r)$-function in (4.13) for $\alpha = 1202$ m^{-1}, together with a possible weight-function of a 10 element 50 mm annular array transducer. In this example, the elements are cut on the zero crossings of the Bessel function, J_0, and the maximum values within the boundaries of the elements are used as weights. The average value could also be used.

The lateral beamwidth of the Bessel beam is given by the width of the mainlobe of the Bessel-function in (4.13). A common measure of the lateral beamwidth is the FWHM (full width half maximum), which is the width of the mainlobe at half the peak value (-6 dB). We have to solve

$$J_0(\alpha r) = 0.5 \qquad (4.23)$$

which gives $\alpha r = 1.52$. The FWHM for the Bessel beam is therefore

$$\text{FWHM}_B = 2r = \frac{3.04}{\alpha} \tag{4.24}$$

Depth of field of the Bessel beam is

$$\text{DOF}_B = \frac{R}{\tan \phi} \tag{4.25}$$

where ϕ is given by (4.22). This expression can be written as [12]

$$\text{DOF}_B = R\sqrt{\left(\frac{2\pi}{\alpha\lambda}\right)^2 - 1} \tag{4.26}$$

4.4   X waves

In section 4.2 we saw that the Axicon beam represents a non-dispersive wave, and presented an approximate expression for the acoustic field generated by an Axicon transducer. Due to the nondispersive behavior of this acoustic field, we know that with a multiple-frequency pulse driven from this transducer, the generated beam would still be limited diffracting for a finite distance. This brings us to the next family of nondiffracting beams, the X waves. The X waves are nondiffracting pulses containing multiple frequencies, and the non-dispersive property of the Axicon beam is exploited. To generate a pulse, we need infinite bandwidth. In terms of mathematics, we integrate over an infinite number of frequencies. If we in (4.2) let $T(k) = B(k)e^{-a_0 k}$, and let the other functions be as those of the Axicon beam, we get

$$\mathbf{p}_{X_n} = e^{in\theta} \int_0^\infty B(k) J_n \left(kr \sin \zeta\right) e^{-k[a_0 - i(z \cos \zeta - ct)]} dk \tag{4.27}$$

which is the nth-order X wave. This expression represents a broadband, nondiffracting pulse, and is nothing but an integration over the nth-order Axicon beam, multiplied by $B(k)e^{-a_0 k}$. Realized with infinite aperture, it will preserve its shape for an infinite distance. In reality, the depth of field is limited, depending on the size of the transducer it is produced with, and the Axicon angle, ζ. $B(k)$ is here the aperture transfer function, which in practice is bandlimited.

If we choose $B(k) = a_0$, (4.27) is a Laplace transform of the function $J_n(kr \sin \zeta)$, multiplied by $a_0 e^{in\theta}$. From [8], we have that

$$\int_0^\infty J_n(\alpha k)e^{-sk} dk = \frac{\alpha^n}{\sqrt{\alpha^2 + s^2}(s + \sqrt{\alpha^2 + s^2})^n} \tag{4.28}$$

where s is any complex number. Substituting $\alpha = r \sin \zeta$ and multiplying with $a_0 e^{in\theta}$ gives us a broadband X wave solution

$$\mathbf{p}_{X_{BB_n}} = \frac{a_0 (r \sin \zeta)^n e^{in\theta}}{\sqrt{M} \left(\tau + \sqrt{M} \right)^n} \tag{4.29}$$

where

$$M = (r \sin \zeta)^2 + \tau^2 \tag{4.30}$$

and

$$\tau = a_0 - i(z \cos \zeta - ct) \tag{4.31}$$

For $n = 0$, the zeroth order X wave becomes

$$\mathbf{p}_{X_{BB_0}} = \frac{a_0}{\sqrt{(r \sin \zeta)^2 + [a_0 - i(z \cos \zeta - ct)]^2}} \tag{4.32}$$

The last equation represents, like the zeroth order Bessel and Axicon beam, an axially symmetric beam, and could therefore be implemented on an annular array transducer. The required bandwidth and aperture size to exactly realize the beam is infinite and therefore impossible, but good approximations can be made with limited bandwidth and finite aperture.

X branches

The reason these beams have been termed X waves, is because the zeroth order X wave given by (4.32) is shaped like an X in a rz-plane through the pulse center. Here $x = r \cos(\theta)$ and $y = r \sin(\theta)$. θ could be any angle between 0 and 2π since the zeroth order X wave solution is independent of θ. Figure 4.3 shows two X waves, with $\zeta = 4°$ and $\zeta = 8°$ respectively, in the xz-plane. With the axial symmetry, the wave forms two cones of pressure, and we see the similarity with the Axicon transducer (but here there are two cones instead of one). The Axicon angle, ζ, affects the resulting X wave in a similar way as the Axicon beam, defining the angle between the cones of pressure and a plane perpendicular to the z-axis. With this we get an intuitive feeling of the depth of field, expecting it to be the same as for the Axicon beam with the same ζ. The absolute value of (4.32) can be written as [8]

$$|\mathbf{p}_{X_{BB_0}}| = \frac{1}{\sqrt[4]{\left[1 + \left(\frac{\sin \zeta}{a_0} \right)^2 r^2 - \left(\frac{\cos \zeta}{a_0} \right)^2 \left(z - \frac{c}{\cos \zeta} t \right)^2 \right]^2 + 4 \left(\frac{\cos \zeta}{a_0} \right)^2 \left(z - \frac{c}{\cos \zeta} t \right)^2}} \tag{4.33}$$

(a)   (b)

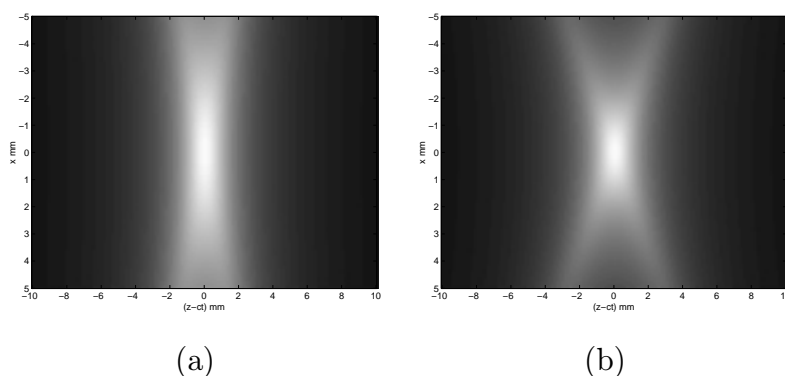Figure 4.3: Two exact zeroth order X waves (a) $\zeta = 4°$ (b) $\zeta = 8°$. $a_0 = 0.05$ mm. $(z - c_1t)$ is the distance away from the pulse center, meaning this is a snapshot in time, the x-axis being the axial distance away from pulse peak, $z = c_1t$

The pressure distribution of the branches of the X waves is obtained when

$$r = \frac{a_0}{\sin \zeta}\sqrt{\left(\frac{\cos \zeta}{a_0}\right)^2\left(z - \frac{c}{\cos \zeta}t\right)^2 - 1} \tag{4.34}$$

where

$$\frac{\cos \zeta}{a_0}\left|z - \frac{c}{\cos \zeta}t\right| \geq 1 \tag{4.35}$$

giving

$$|\mathbf{p}_{\text{X−branches}}| = \frac{1}{\sqrt{2\frac{\cos \zeta}{a_0}\left|z - \frac{c}{\cos \zeta}t\right|}} \tag{4.36}$$

This direction is the slowest descent of the X wave amplitude away from the center and is clearly seen in figure 4.3. From the simulations of bandlimited finite aperture realizations which is presented later, we shall see that the energy in the branches is less than for the broadband infinite aperture case. But the energy in the X branches could lead to image artifacts if the X waves were applied to medical imaging. Lu *et al.* [8] have proposed X wave transmit and dynamic focused reception to reduce the X branch influence.

Causality and propagation speed

With the pulse center, $z = c_1t$, in the center of the plots in figure 4.3, we see that (4.32) is not a causal solution to the wave equation. Two of the
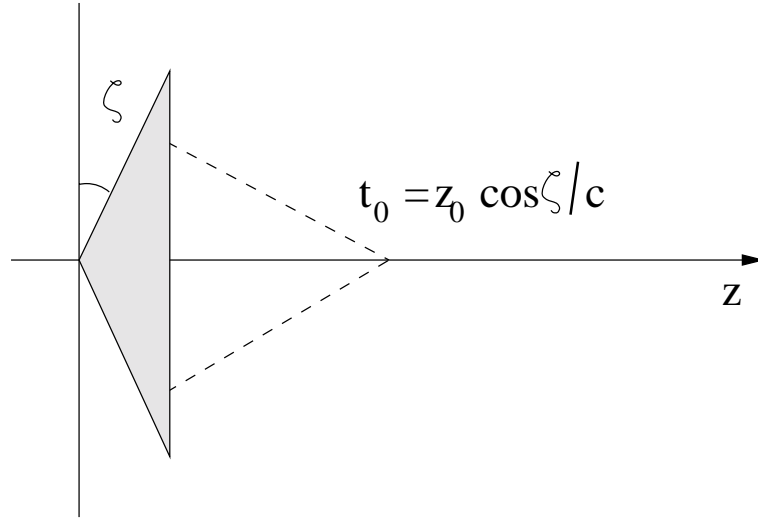
$$t_0 = z_0 \cos\zeta / c$$

Figure 4.4: Illustration of the propagation speed of the pulse center of the X wave. The pulse peaks at time $t_0 = z_0 \cos\zeta/c$, making the X wave a supersonic wave.

X branches travel in front of the pulse center, which has its maximum at $z = c_1 t$, meaning that $\mathbf{p}_{XBB_0}(\vec{r}, t)$ is not zero for $t < 0$. At a given distance, z_0, the X waves extend in time from $t > -\infty$ to $t < \infty$, but $\mathbf{p}_{BBX_0}$ diminishes very fast as $|t|$ increases. In practical applications, they would be truncated in time, and realized with a causal approximation.

Since the speed, $c_1 = c/\cos\zeta$, of the pulse center is greater than c for $\zeta > 0$, the pulse travels faster than the speed of sound, making it a supersonic wave. This seems strange but can be explained by looking at the Axicon transducer. A pulse generated by a conical transducer would peak on the z-axis where the pulses from the lines perpendicular to the cone walls intersect. At large axial distances, the pulse is mainly composed of the intersection of the signals from large radii. Due to the shape of the transducer, the wavefront is advanced as the radius becomes larger, so the pulses intersect on the z-axis at time, $t_0 = z_0 \cos\zeta/c$ as seen in figure 4.4. So the pulse center travels at speed, $c_1 = c/\cos\zeta$, which is greater than speed of sound, even though the radiated energy travels at speed c. The same is the case for the X waves. The wavefront is advanced in time as the radius becomes larger, and at large z it is the energy from each side of the transducer that constructs the X wave.

Depth of field

Like the Axicon beam, the X waves are also defined by the Axicon angle, ζ, and the depth of field is expected to be the same as for the Axicon from a geometrical point of view. Analytically, it can be found from the depth of field of the Bessel beam. The Fourier transformation of the zeroth order X wave is (see chapter 5)

$$\mathbf{P}(\vec{r}, \frac{\omega}{c}) = \frac{2\pi}{c} B\left(\frac{\omega}{c}\right) J_0\left(\frac{\omega}{c} r \sin\zeta\right) H\left(\frac{\omega}{c}\right) e^{-\frac{\omega}{c}(a_0 - iz\cos\zeta)} \qquad (4.37)$$

where

$$H\left(\frac{\omega}{c}\right) = \begin{cases} 1, & \omega \geq 0 \\ 0, & \omega < 0 \end{cases} \qquad (4.38)$$

From (4.37) wee see that the acoustic field of an X wave is, for any frequency, ω_0, a continuous field shaded by a J_0 Bessel function

$$S(\omega_0) J_0(\alpha r) \qquad (4.39)$$

where

$$S(\omega_0) = \frac{2\pi}{c} B\left(\frac{\omega_0}{c}\right) H\left(\frac{\omega_0}{c}\right) e^{-\frac{\omega_0}{c}(a_0 - iz\cos\zeta)} \qquad (4.40)$$

and

$$\alpha = \frac{\omega_0}{c} \sin\zeta \qquad (4.41)$$

Substituting (4.41) in the depth of field of the Bessel beam, given by (4.26), we get the the depth of field of the zeroth order X wave

$$\mathrm{DOF}_{X_0} = R\sqrt{\left(\frac{\omega_0}{\alpha c}\right)^2 - 1} \qquad (4.42)$$

$$= \frac{R}{\tan\zeta} \qquad (4.43)$$

which is independent of ω_0, and is what we expected from geometry. This means that if we have a smaller Axicon angle, ζ, we have a larger depth of field.

Lateral and axial beamwidth

At the plane $z = \frac{ct}{\cos\zeta}$, which is the lateral pressure distribution through the pulse center of the X wave, we have from (4.32)

$$|\mathbf{p}_{XBB_0}| = \frac{1}{\sqrt{1 + \left(r\frac{\sin\zeta}{a_0}\right)^2}} \tag{4.44}$$

To find the -6 dB lateral beamwidth, we solve $|\mathbf{p}_{XBB_0}| = 0.5$, which gives

$$\text{FWHM}_{XBB_0} = 2r = \frac{2\sqrt{3}a_0}{\sin\zeta} \tag{4.45}$$

On the line $r = 0$, which is the axial pressure distribution of the X waves, we have from (4.32)

$$|\mathbf{p}_{XBB_0}| = \frac{1}{\sqrt{1 + \left(\frac{\cos\zeta}{a_0}\right)^2\left(z - \frac{c}{\sin\zeta}t\right)^2}} \tag{4.46}$$

The -6 dB axial beamwidth is found to be

$$2\left|z - \frac{c}{\cos\zeta}t\right| = \frac{2\sqrt{3}a_0}{\cos\zeta} \tag{4.47}$$

From (4.43) and (4.45), we see that there is a tradeoff between depth of field and lateral resolution. Larger ζ gives a larger depth of field, but the lateral resolution is decreased. Larger ζ will also increase the axial resolution. Smaller values of a_0, will increase both the lateral and axial resolution, but requires more bandwidth. This can be seen from the Fourier transform in (4.37). When a_0 is small, the term $e^{-a_0\frac{\omega}{c}}$ diminishes slower and requires greater values of ω.

4.5   Bessel beam with frequency adjusted α

In section 4.3 the Bessel beam was shown to be as dispersive wave, since the speed of propagation is dependent on frequency, as expressed in (4.15). From (4.22), α can be expressed by ϕ as

$$\begin{aligned} \alpha &= \sin(\phi)\frac{2\pi}{\lambda} \\ &= k\sin(\phi) \end{aligned} \tag{4.48}$$

From (4.14), β^2 then becomes

$$
\begin{aligned}
\beta^2 \ &= \left(\tfrac{\omega}{c}\right)^2 - \alpha^2 \\
&= k^2 - \alpha^2 \\
&= k^2 - k^2 \sin^2(\phi) \\
&= k^2 \left(1 - \sin^2(\phi)\right)
\end{aligned}
\tag{4.49}
$$

which gives

$$
\beta = k \cos(\phi)
\tag{4.50}
$$

By choosing ϕ constant, α is adjusted for each frequency if more than one frequency is transmitted, giving a nondispersive wave with speed of propagation

$$
\begin{aligned}
c_1(k, \phi) \ &= \tfrac{\omega}{\beta} \\
&= \tfrac{\omega}{k \cos(\phi)} \\
&= \tfrac{c}{\cos(\phi)}
\end{aligned}
\tag{4.51}
$$

Inserting (4.48) and (4.50) into the expression for the Bessel beam, we get

$$
\mathbf{p} = J_n \left(k \sin(\phi)r\right) e^{i(kz \cos(\phi) - \omega t + n\theta)}
\tag{4.52}
$$

which is the expression for the Axicon beam with ϕ as the Axicon angle. From section 4.4 we have seen how to get from the Axicon solution to the X wave solution, so we see there is a close connection between the limited diffraction beams.

4.6   Other solutions

By choosing $T(k) = B(k)e^{-a_0 k}$ to obtain the exact X wave solution given by (4.29), the weighting on the frequencies diminishes exponentially, so there is little energy in the high frequency components making the X waves realizable with finite bandwidth. But this means that not all available bandwidth is used, even when limiting the bandwidth by choosing $B(k)$ an appropriate window function. If we assume infinite bandwidth, as for (4.29), an analytical expression could be found which does not include the exponential decay. If $T(k) = 1$ we get a solution from (4.28)

$$
\mathbf{p} = \frac{(r \sin \zeta)^n e^{in\theta}}{\sqrt{M} \, (\tau + M)^n}
\tag{4.53}
$$

where

$$M = (r \sin \zeta)^2 + \tau^2 \tag{4.54}$$

and

$$\tau = -i(z \cos \zeta - ct) \tag{4.55}$$

the last expression for τ differs from the X wave solution. For $n = 0$, the solution is given by

$$\mathbf{p} = \frac{1}{\sqrt{(r \sin \zeta)^2 + [-i(z \cos \zeta - ct)]^2}} \tag{4.56}$$

When $r = 0$ and $t = (z \cos \zeta)/c$, there is a singularity, but this does not matter in practice where the bandwidth is limited. Since (4.56) fits in the general limited diffraction solution given by (4.2), it is a valid solution of the wave equation, since the only difference from the X wave is that we set $T(k) = 1$. The problem with this solution, is that a realization with finite bandwidth and aperture, would be a bad approximation to the exact solution. We shall see in the next chapter that finite bandwidth and aperture realizations of the X waves are close to the exact solution within the depth of field. Figure 4.5 shows two realizations with finite aperture and finite bandwidth, where the dotted line represents the previously discussed solution, and the solid line is an X wave with $a_0 = 0.05$ mm. We see that the two plots are almost identical, the X wave is slightly broader but has lower sidelobes. These realizations have a central frequency of 2.5 MHz, and the figure shows that this is the main parameter, together with ζ, that gives the beamwidth as long as a_0 is chosen small enough.
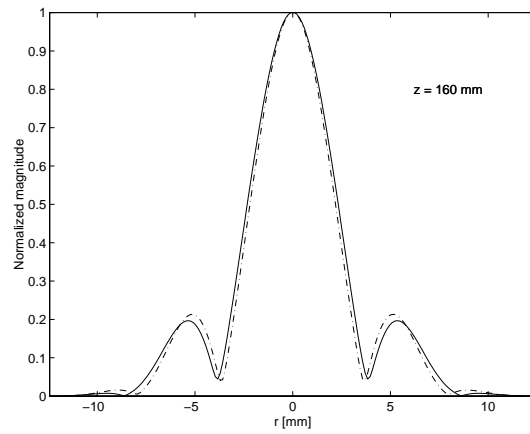
Figure 4.5: Example of the two finite aperture and finite bandwidth realizations with $a_0 = 0$ (dotted line) and $a_0 = 0.05$ mm (solid line)

Chapter 5

Simulation and realization of limited diffraction beams

5.1   Simulation

5.1.1   Simulation of the Bessel beam

Simulation of the Bessel beam with continuous wave excitation could be done by either method described earlier. The time domain version of the Rayleigh-Sommerfeld integral (3.22) could be applied, or one of the methods involving discrete transforms. The zeroth order Bessel beam has circular symmetry, so the SSC-method based on the discrete Hankel transform has been used here. From (4.13) we see that the Bessel beam is simply a plane wave weighted by a Bessel function, so the source function is

$$s(r) = J_0(\alpha r) \tag{5.1}$$

in the algorithm. Since the spatial extent of the field must be larger than the size of the transducer, the samples of the source are set to zero when $r > a$, where a is the radius of the transducer.

To simulate pulsed Bessel beam excitation, a broadband beam is required. The frequency version of the Rayleigh integral could then be used, or the SSC-algorithm with many harmonics. The source-function would be the same for each harmonic, but a window could be applied to approximate the transfer function of a real transducer. This will be described in the next section, where methods for simulating X waves are presented.
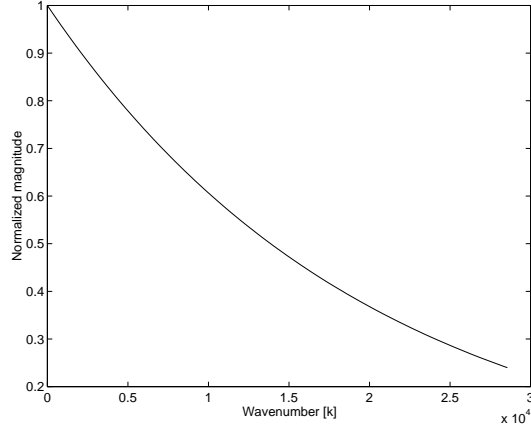
Figure 5.1: Temporal Fourier transform of zeroth-order X wave at the point $(r, z) = (0, 0)$, $B(k) = a_0$, $a_0 = 0.05$ mm. Due to the exponential factor, $e^{-\frac{\omega}{c}a_0}$, the contributions from higher frequencies are less significant.

5.1.2 Simulation of X waves

The family of X waves given by (4.27) can be written as

$$\mathbf{p}_{X_n}(\vec{r}, t) = \frac{1}{2\pi} \int_{-\infty}^{\infty} \left[\frac{2\pi}{c} e^{in\theta} B\left(\frac{\omega}{c}\right) J_n\left(\frac{\omega}{c} r \sin\zeta\right) H\left(\frac{\omega}{c}\right) e^{-\frac{\omega}{c}(a_0 - iz\cos\zeta)} \right] e^{-i\omega t} d\omega \tag{5.2}$$

which is an inverse Fourier transform of

$$\mathbf{P}_{X_n}\left(\vec{r}, \frac{\omega}{c}\right) = \frac{2\pi}{c} e^{in\theta} B\left(\frac{\omega}{c}\right) J_n\left(\frac{\omega}{c} r \sin\zeta\right) H\left(\frac{\omega}{c}\right) e^{-\frac{\omega}{c}(a_0 - iz\cos\zeta)} \tag{5.3}$$

$H(\frac{\omega}{c})$ is the Heaviside step function,

$$H\left(\frac{\omega}{c}\right) = \begin{cases} 1, & \omega \geq 0 \\ 0, & \omega < 0 \end{cases} \tag{5.4}$$

From (5.3) we see that the bandwidth required for the X waves is infinite, but there is little energy in the high frequency components of the waves, making them realizable with finite bandwidth.

At the plane $z = 0$, which could be the surface of a transducer, the temporal Fourier transform becomes

$$\mathbf{P}_{X_n}\left(r, \theta, \frac{\omega}{c}\right) = \frac{2\pi}{c} B\left(\frac{\omega}{c}\right) J_n\left(\frac{\omega}{c} r \sin\zeta\right) H\left(\frac{\omega}{c}\right) e^{-\frac{\omega}{c}a_0 + in\theta} \tag{5.5}$$
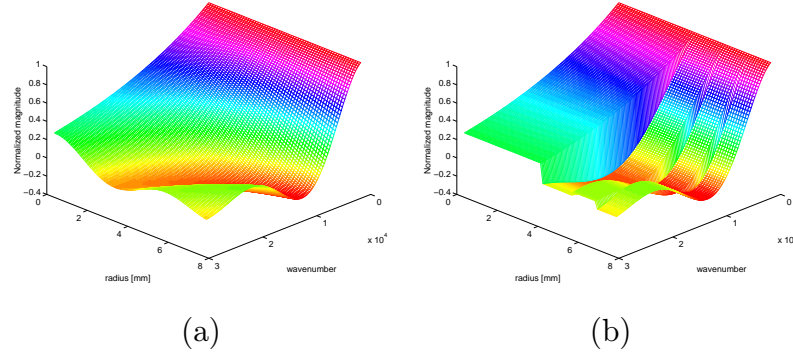
Figure 5.2: Temporal Fourier transform of zeroth-order X wave at the line $(y, z) = (0, 0)$. X-axis is the wavenumber, k, and Y-axis is the radius of the aperture (a) Continuous aperture (b) Aperture discretized to 4 elements.

A plot of $\mathbf{p}_{X_0}$ with $n = 0$, $B(k) = a_0$ and $r = 0$ is shown in figure 5.1. Note that $J_0 = 1$ for all k since $r = 0$, so the spectrum diminishes exponentially, depending on the parameter a_0. We now see why smaller a_0 gives better axial and lateral resolution. When a_0 is small, $e^{-\frac{\omega}{c} a_0}$ in (5.3) diminishes slower, so there is more energy in the high frequency components, giving a narrower beam. $\mathbf{P}_{X_0}$ for different lateral distances is shown in figure 5.2 (a). This could be the temporal Fourier transform at the surface of a transducer with radius 7.5 mm.

To simulate a realization of an X wave with finite aperture and bandwidth, the frequency-domain version of the Rayleigh-Sommerfeld diffraction formula could be used. The Fourier transform of an nth-order X wave at the plane $z = 0$, is given by (5.5). By inserting this expression into (3.23), the diffraction formula for X waves becomes

$$
\begin{aligned}
\hat{\mathbf{P}}_{X_n}(\vec{r_0}, \omega) &= \frac{1}{i\lambda} \int_0^R \int_0^{2\pi} E_n(\vec{r_1}, \omega) e^{ikr_{01}} \frac{z}{r_{01}^2} r_1 d\theta dr_1 \\
&+ \frac{1}{2\pi} \int_0^R \int_0^{2\pi} E_n(r_1, \omega) e^{ikr_{01}} \frac{z}{r_{01}^3} r_1 d\theta dr_1
\end{aligned}
\tag{5.6}
$$

where

$$
E_n(\vec{r_1}, \omega) = \frac{2\pi}{c} J_n \left(\frac{\omega}{c} r \sin \zeta \right) H \left(\frac{\omega}{c} \right) e^{-\frac{\omega a_0}{c} + in\theta}
\tag{5.7}
$$

Since a practical transducer has limited bandwidth, the transfer function is also approximated. This is done by limiting the bandwidth of $B(k)$ in (5.5). To approximate the bandwidth of a real transducer, a Blackman window

function [8] could be used. $B(k)$ is then given by

$$B(k) = \begin{cases} a_0 \left(0.42 - 0.5 \cos \frac{\pi k}{k_0} + 0.08 \cos \frac{2\pi k}{k_0} \right), & 0 \leq k \leq 2k_0 \\ 0, & \text{otherwise} \end{cases} \tag{5.8}$$

The simulation is now done by calculating (5.6) for all frequencies covered by the Blackman window, at all the spatial positions, $\vec{r_0}$, where you want to find the acoustic pressure. For each spatial point, an inverse Fourier transform of $\hat{\mathbf{P}}_{X_n}(\vec{r_0}, \frac{\omega}{c})$ is done, giving the prediction of diffraction in space and time, $\hat{\mathbf{p}}_{X_n}(\vec{r_0}, t)$.

Alternatively, the SSC-algorithm could be used for simulating X waves of zeroth order. This requires a multiharmonic source which is obtained by sampling the Fourier transform in (5.5) for $n = 0$, and use the samples as Fourier coefficients, which results in a Fourier series for each lateral sample. Inclusion of a Blackman window for approximation of the bandwidth of a real transducer is done by weighting each Fourier coefficient by the corresponding value of $B(k)$. The response function $h(r, z)$, must be calculated for each harmonic component, resulting in i discrete functions, $h_i(z, r)$, where i is the ith harmonic.

Since a practical transducer has a finite number of elements the spectrum would not be continuous along the lateral axis as in figure 5.2 (a). To simulate X waves produced by an annular array, the lateral axis is discretized according to where the rings are cut as shown in figure 5.2 (b). This will be further explained in the next section.

5.2   Realization

5.2.1   Realization of the Bessel beam

As mentioned, the zeroth order Bessel beam is just a plane wave shaded by a Bessel function, $J_0(\alpha r)$. To realize the beam, an annular array could be used because of the circular symmetry. Applying an annular array means that the aperture shading function is discretized because of the finite number of elements. The aperture weights are samples of $J_0(\alpha r)$, and if possible, the rings of the transducer would be cut at the zeros of this Bessel function. We see that for a broadband pulse excited from a Bessel transducer, the aperture weighting is the same for each frequency. This is why the Bessel beam is a dispersive wave, as shown in the previous chapter.

Element no.	1	2	3	4	5	6	7	8	9	10
Radius (mm)	2	4.59	7.2	9.81	12.4	15	17.6	20.3	22.9	25
r	0	3.295	5.895	8.505	11.105	13.7	16.3	18.95	21.6	23.95

Table 5.1: The radii of the annular elements in example 1 and 3. The value r is used to calculate the signals driven from each element to produce the X wave in example 3.
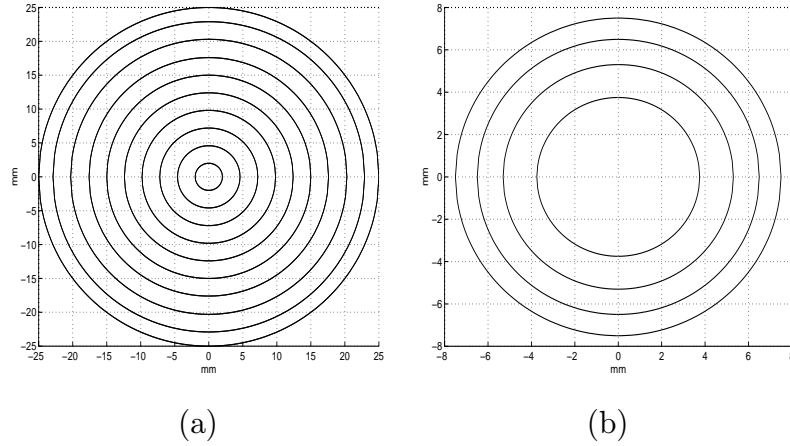

(a)   (b)

Figure 5.3: (a) 10 element annular array transducer (example 1 and 3). (b) 4 element equal area annular array transducer (example 2 and 4).

Example 1: 50 mm 2.5 MHz transducer

Lu *et. al*[11] have designed a 50 mm 2.5 MHz Bessel transducer, and experimentally verified results from computer simulations. The transducer is an annular array consisting of 10 rings where the rings are cut at the zeros of $J_0(\alpha r)$ in (4.13). The parameter, α, is chosen as 1202 m^{-1}, which gives a Bessel-function with 10 lobes. Table 5.1 shows the resulting radius of each ring, and figure 5.3 (a) shows the annular array.

From (4.24) the theoretical lateral beamwidth is

$$\text{FWHM}_B = \frac{3.04}{1202 \text{ m}^{-1}} = 2.53 \text{ mm} \tag{5.9}$$

The theoretical depth of field is given by (4.26)

$$\text{DOF}_B = 25 \text{ mm} \sqrt{\left(\frac{2\pi}{1202 \text{ m}^{-1}\lambda}\right)^2 - 1} = 216 \text{ mm} \tag{5.10}$$

Figure 5.4 shows simulations of the acoustic field generated by this config-
uration with continuous wave excitation. Figure 5.4 (a) shows the initial
field given to the SSC-algorithm. We see that the chosen parameters give
a Bessel-function with ten lobes within the boundaries of the transducer,
where the annular elements are cut at the end of each lobe. The solid line
represent the weighting of each element, giving a discrete approximation to
the exact aperture shading. Figure 5.4 (b) shows the acoustic pressure from
2 to 400 mm. The depth of field is close to what was predicted by theory for
both the exact and discretized shading (216 mm), but we see that the finite
element approximation has some near-field artifacts. Figure 5.4 (c) and (d)
shows the lateral field distribution at two distances, z = 100 and z = 160
mm. In theory the lateral distribution should be the $J_0(\alpha r)$ function. The
finite aperture realizations show differences in the sidelobes but this is of no
importance (note that the absolute value is plotted here). Still, the main
lobe has roughly the same width in the two plots, and from figure 5.5 we see
that both the exact and finite element case is limited diffracting throughout
the depth of field. The beamwidth is also close to the predicted value given
by the width of the main lobe in the Bessel-function.

Example 2: 15 mm 3.5 MHz transducer

The diameter of the transducer in example 1 is relatively large, and is too
large for applications like cardiology. Holm [9] has simulated a Bessel beam
generated by a 15 mm, 3.5 MHz equal area annular array transducer with 4
elements, which is a more realistic example for practical applications. This
type of transducer is commonly used, and is preferred for dynamic focusing.
The radius of element n for this transducer can be found by the formula [13]

$$r_n = R\sqrt{\frac{n}{N}} \tag{5.11}$$

where N is the total number of elements. The result of the equal area of each
ring is a large radius of the inner as seen in figure 5.3 (b). The parameters
are therefore chosen so that the first zero of the Bessel-function in (4.13) is at
the end of the first ring. The distance to the first zero of the Bessel function
is 2.404 [12]. The first zero is therefore located at

$$\alpha r_1 = 2.404 \tag{5.12}$$

where r_1 is the radius of the first ring, calculated by (5.11). α is found by
solving (5.12) which gives the value 641.3 m^{-1}. This gives the theoretical
beamwidth and depth of field as

$$\text{FWHM}_B = \frac{3.04}{641.3 \text{ m}^{-1}} = 4.7 \text{ mm} \tag{5.13}$$
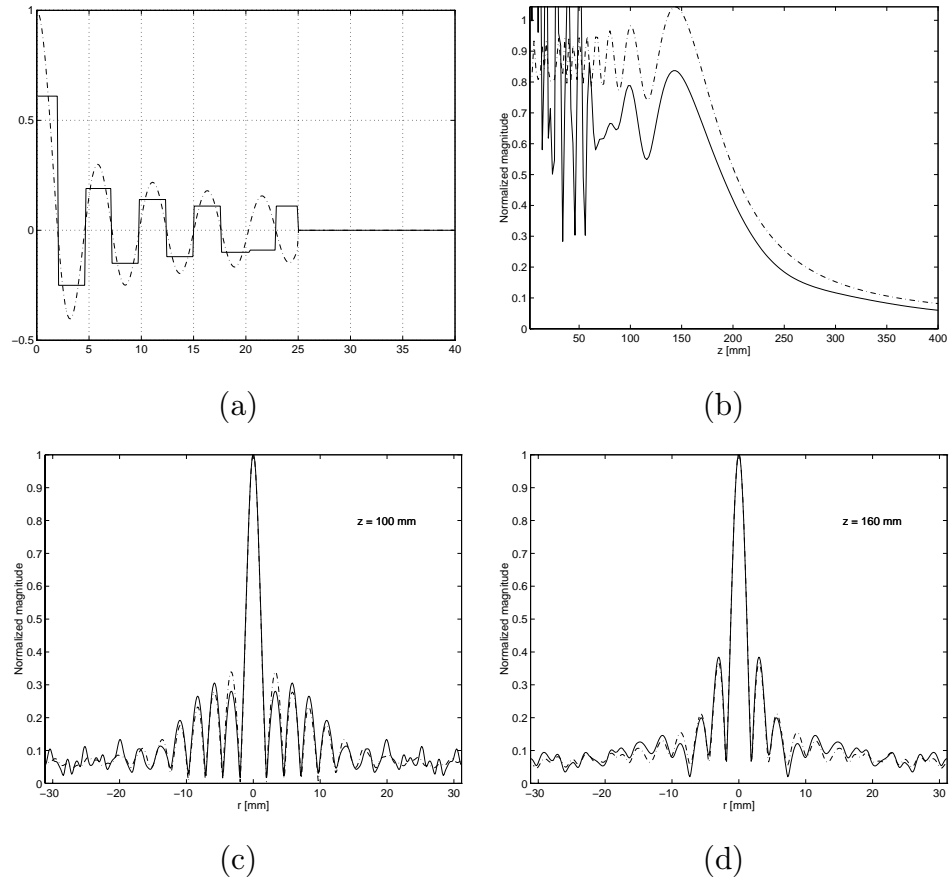
(a)

(b)

(c)

(d)

Figure 5.4: Bessel beam in example 1. Dotted line represents exact aperture shading, and solid line is the 10 element annular array approximation. (a) Initial field given to the SSC algorithm (b) Acoustic pressure from $z = 2$ to 400 mm (c) Lateral beamprofile at $z = 100$ mm (d) Lateral beamprofile at $z = 160$ mm

and

$$\text{DOF}_B = 7.5 \text{ mm} \sqrt{\left(\frac{2\pi}{641.3 \text{ m}^{-1} \lambda} \right)^2 - 1} = 167 \text{ mm} \qquad (5.14)$$

Figure 5.6 (a) shows the source function in the SSC algorithm. We see that this configuration gives a Bessel function with less than two lobes, where the radius of the first element determines the first zero. This gives a broad beam, but also a large depth of field, as predicted by theory. Figure 5.6 (b) shows the acoustic pressure along the z-axis from 1-200 mm. The depth of field agrees well with theory, but again the finite element realization shows some near-field artifacts. The lateral plots in 5.6 (c) and (d), and the images in figure 5.7 shows that the beamwidths for both the continuous shading and annular array approximation are close the predicted values, despite that less than two lobes of the Bessel function are included in the approximation.

5.2.2 Realization of X waves

While the signals driven from the transducer to generate a Bessel beam is the same for all lateral distances, the X waves are special since different signal are excited for different r. So to realize the X waves with physical devices, we must find which signals to drive from the different points on the transducer. This can be found by calculating (4.29) at the plane $z = 0$ for different r and θ. Ideally the transducer would be divided into an infinite number of elements, and different signals would be driven from each element. This is of course not possible, so we have to approximate the X waves with a finite number of elements.

    If we let $n = 0$, we get the expression for the zeroth order X wave given by (4.32). This expression is independent of the angle θ, the zeroth order X wave is therefore an axially symmetric wave. An annular array transducer could therefore be used to realize this wave, driving different signals from each ring of the transducer. At the plane $z = 0$, (4.32) becomes

$$\mathbf{P}_{X_0}(r, \theta, 0, t) = \frac{a_0}{\sqrt{(r \sin \zeta)^2 + (a_0 + ict)^2}} \qquad (5.15)$$

If the annular array transducer is divided into N rings, the signal driven from each ring is calculated by the real part of (5.15) for N different radii. The radii used in the calculations, could be the average radius of each ring. The parameters a_0 and ζ also have to be chosen depending on the configuration of the transducer and the depth of field we want. a_0 would be chosen as small as possible, since that gives both better axial and lateral resolution, but the

bandwidth of the transducer limits how small a_0 can be chosen. ζ is chosen depending on the depth of field we want, but larger depth of field results in a decrease in lateral resolution.

Example 3: 2.5 MHz 50 mm 10 element annular array transducer

This example uses the same transducer as for the Bessel beam in example 1. Lu *et. al*[14] have simulated and experimentally verified a zeroth order X wave generated by this transducer. The transducer had a bandwidth of 50% of the central frequency of 2.5 MHz. Since each element is excited by a broadband signal, the bandwidth of the transducer is approximated by a Blackman window when calculating the acoustic fields in the simulations. The parameters were chosen as $a_0 = 0.05$ mm and $\zeta = 4°$. The signals driven from each element are calculated by the the real part of (5.15), with r as the average radius of each element. Table (5.1) shows the radius of the annular elements and the value, r, used to calculate the waveforms driven from them. Figure 5.3 (a) shows the annular array transducer in this example, and figure 5.8 shows the signals driven from each element.

The theoretical depth of field with this configuration, given by (4.43), is

$$\text{DOF}_X = \frac{25 \text{ mm}}{\tan(4°)} = 358 \text{ mm} \tag{5.16}$$

the -6 dB axial beamwidth, given by (4.47), is

$$\text{Axial BW}_X = \frac{0.05 \text{ mm } 2\sqrt{3}}{\cos(4°)} = 0.17 \text{ mm} \tag{5.17}$$

and the -6 dB lateral beamwidth, given by (4.45), is

$$\text{FWHM}_X = \frac{0.05 \text{ mm}2\sqrt{3}}{\sin(4°)} = 2.5 \text{ mm} \tag{5.18}$$

Figure 5.9 (a) and (b) shows the source functions in the SSC-algorithm for each harmonic component used to simulate these X wave realizations. The calculation uses 128 harmonics, but the field in the figure has been truncated to 32 harmonics to make it easier to see the curves. The figures are the sampled X wave Fourier transformations shaded by a Blackman window to approximate the bandwidth of the transducer, where figure 5.9 (a) represents exact aperture shading and figure 5.9 (b) is the finite element approximation. We see that this gives, unlike the Bessel beam, a different weight for each frequency, which is the reason why the X waves are non-dispersive. The weight for each harmonic component is adjusted to make the focusing area

equal, where for the Bessel beam the equal weighting gives different focus
and different speed of each frequency if exciting a broadband signal.

Figure 5.10 (a) shows the pulse peaks from z = 10 mm to z = 60 mm
of the simulated X waves. Note that because of the supersonic property of
the X waves, the pulse peaks at time, $t = z \cos(\zeta)/c$, which was explained
in the previous chapter. The figure shows good correspondence with the
predicted depth of field, but the pressure of the finite element approximation
is high near the source. Figure 5.10 (b) shows a snapshot of the X waves in
time at distance z = 90 mm. The time axis has been converted to distance to
measure the axial beamwidth. The axial beamwidth is far from the predicted
value of 0.17 mm, which is not surprising, since the wavelength of the highest
frequency component within the bandwidth of the transducer ($2f_0$ where f_0
is the central frequency), is about 0.3 mm. What we also see from this plot,
is the presence of edge waves, seen to the right of the pulse peak. They are
especially large for the finite element approximation, but also present for the
continuous aperture shading, but here they are well separated. The edge
waves are caused by the sharp truncation of the pressure at the edge of the
transducer, and can be reduced by proper apodization techniques. Lu *et.
al*[8] shows and example of edge wave reduction by weighting the aperture
with a truncated Blackman window. The side effect is reduced depth of field,
because the effective aperture size is decreased.

Figure 5.10 (c) and (d) shows the lateral field distributions at two dif-
ferent distances, z = 100 mm and z = 160 mm. Both plots have about the
same beamwidth, and figure 5.11 (a) and (c) shows that the beamwidth is
approximately the same within the depth of field. The beam is not as nar-
row as predicted by theory, which is because a_0 is chosen too small to get
the finite bandwidth realizations to agree with the theoretical beams. Still,
by choosing a_0 smaller, the available bandwidth is used more effectively, as
discussed in the previous chapter where an example of a beam with $a_0 = 0$
was shown. Figure 5.11 (b) and (d) show the lateral distributions in time
at z = 90 mm. For both simulations we clearly see the X branches, and the
edge waves are also obvious for the finite element realization.

Example 4: 3.5 MHz, 15 mm, 4 element equal-area annular array transducer

The same transducer as in example 2 is used for simulating a possible realiza-
tion of a zeroth-order X wave. The parameter, $a_0 = 0.05$ mm and ζ is chosen
so that the first zero of $J_0(k_0 r \sin \zeta)$ in (4.32) appears at the end of the first
ring for the central frequency, $k_0 c/2\pi = 3.5$ MHz. This means solving

$$k_0 r_1 \sin \zeta = 2.404 \tag{5.19}$$

which, gives $\zeta = 2.57°$, which is the same value as the corresponding ϕ for the Bessel beam. The waveforms driven from each element are shown in figure 5.12. They are calculated by (5.15) with r as the average radii of each element. Simulations of the acoustic field generated by this transducer are shown in figure 5.13 and 5.14.

The theoretical depth of field (-6 dB) is

$$\mathrm{DOF}_{X_0} = \frac{7.5 \text{ mm}}{\tan(2.57°)} = 167 \text{ mm} \tag{5.20}$$

From figure 5.13 (a), we see that both the continuous and stepwise aperture simulations are close to this value. The finite element example has larger magnitude which is caused by the large inner element. In figure 5.13 (b) we see a snapshot in time of the pulse at z = 80 mm. The time axis has also here been converted to distance to measure axial beamwidth, which from theory is predicted as

$$\frac{0.05 \text{ mm} 2\sqrt{3}}{\cos(2.57°)} = 0.17 \text{ mm} \tag{5.21}$$

which is the same as the previous example. The axial beamwidth is neither as narrow as the theoretical predictions, but is closer than the previous example, due to the increase in central frequency. The wavelength of the maximum frequency component is now 0.22 mm. The edge waves are not present to the same degree as in example 3 for the finite element approximation, and the two plots in figure 5.13 (b) are now almost identical.

Figure 5.13 (c) and (d) shows the lateral field distribution at z= 60 mm and z = 100 mm, which shows that the beamwidth is about the same as the theoretical, given by

$$\mathrm{DOF}_X = \frac{0.05 \text{ mm} 2\sqrt{3}}{\sin(2.57°)} = 3.86 \text{ mm} \tag{5.22}$$

This means that a_0 in this example is a better choice to get agreement between theory and realizations.

5.3   Discussion

From the previous examples we have seen that both the Bessel beam and X wave can be well approximated by finite aperture realizations within the depth of field. The finite element realizations are again good approximations to the exact aperture shading, despite some near-field artifacts and difference

in pressure along the direction of propagation. The lateral field distribution shows good agreement, regarding beamwidth and sidelobes. Note that the Bessel beams and X waves simulated here are not comparable, since the simulations of the Bessel beam assumes continuous wave excitation, while the X wave is a broadband pulse. The effect of pulsed Bessel beam excitation could also be simulated by using a multiharmonic source function, but this has not been studied here.
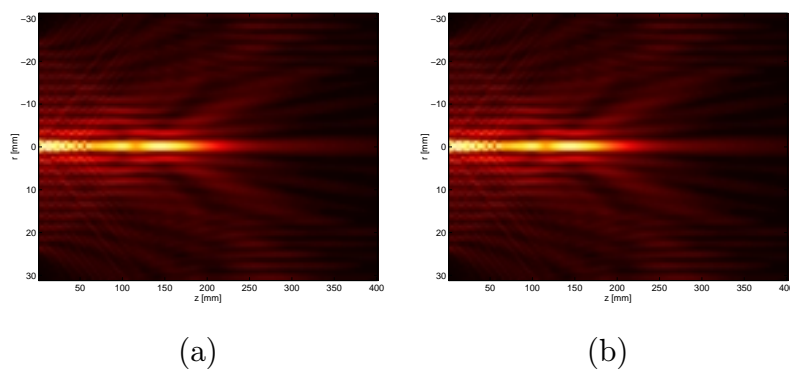
(a)   (b)

Figure 5.5: Bessel beam in example 1 from z=2-400 mm(a) Exact aperture shading (b) Aperture divided into 10 annular elements
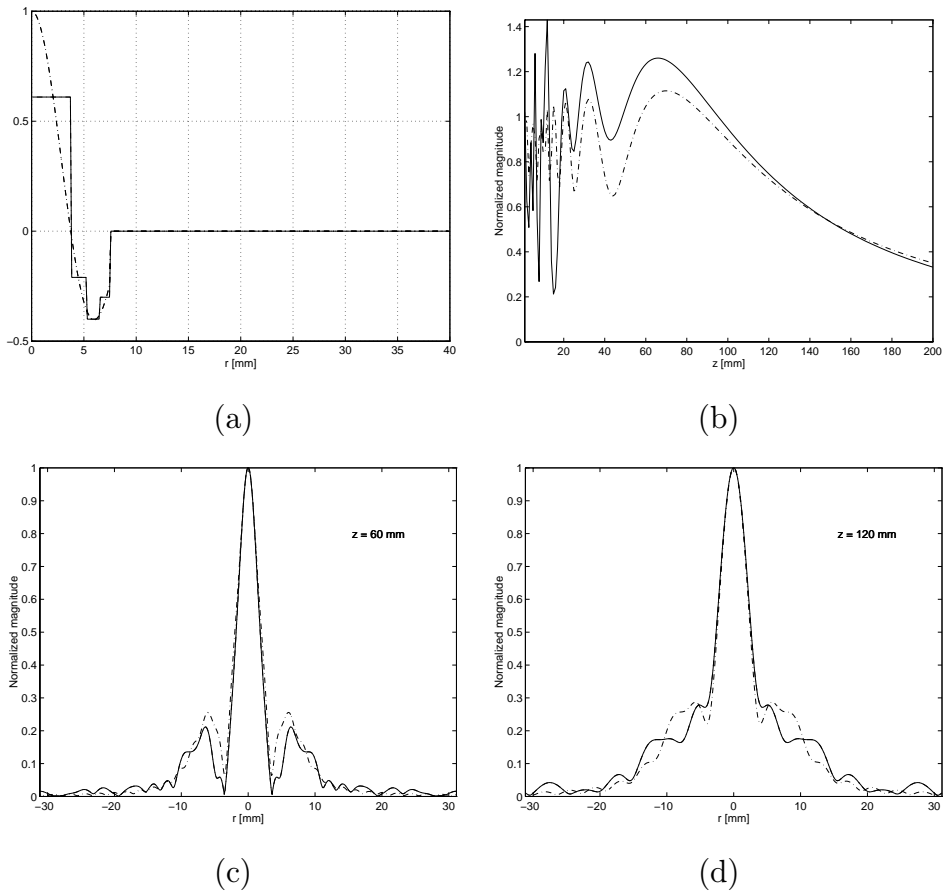
Figure 5.6: Bessel beam in example 2. Dotted line represents exact aperture shading, and solid line is the 4 element annular array approximation. (a) Initial field given to the SSC algorithm (b) Acoustic pressure from $z = 1$ to 200 mm (c) Lateral beamprofile at $z = 60$ mm (d) Lateral beamprofile at $z = 120$ mm
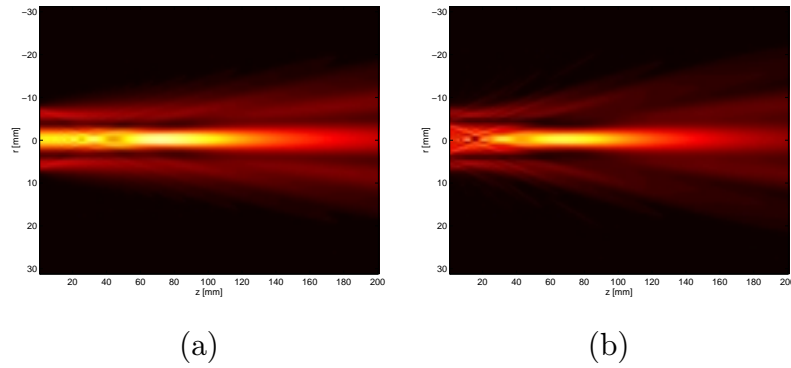
(a) (b)

Figure 5.7: Bessel beam in example 2 (a) Exact aperture shading (b) Aperture divided into 4 annular elements
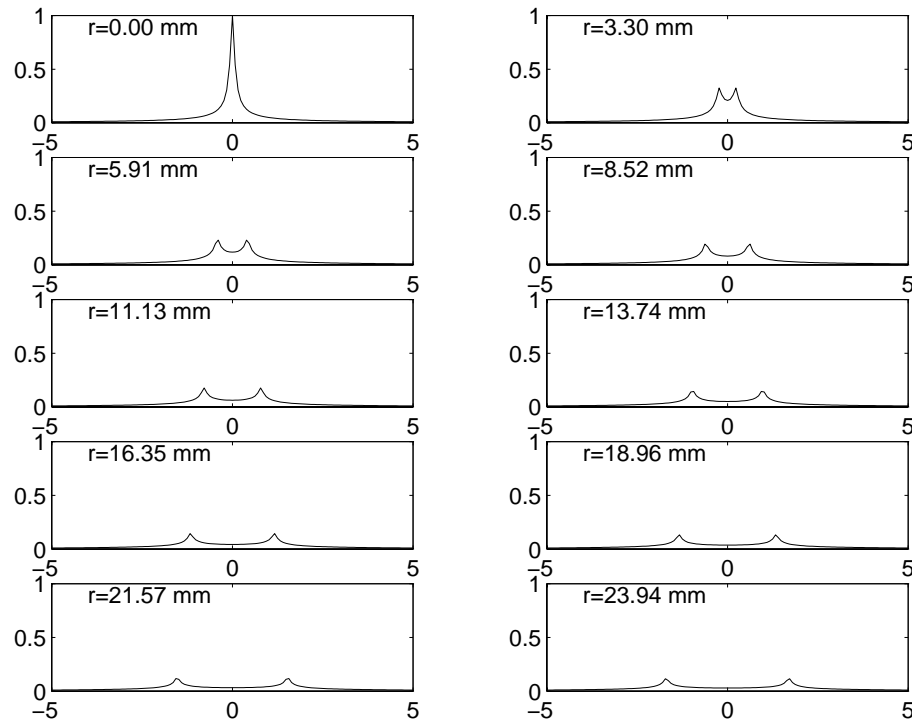

Figure 5.8: The pulses driven from each element of the annular array transducer in figure 5.3 (a). X-axis is time in microseconds (a). The given value, r, for each plot, is the average radius of each ring. This value is used when calculating the waveforms from equation (5.15). The parameters a_0 and ζ are 0.05 mm and 4° respectively.
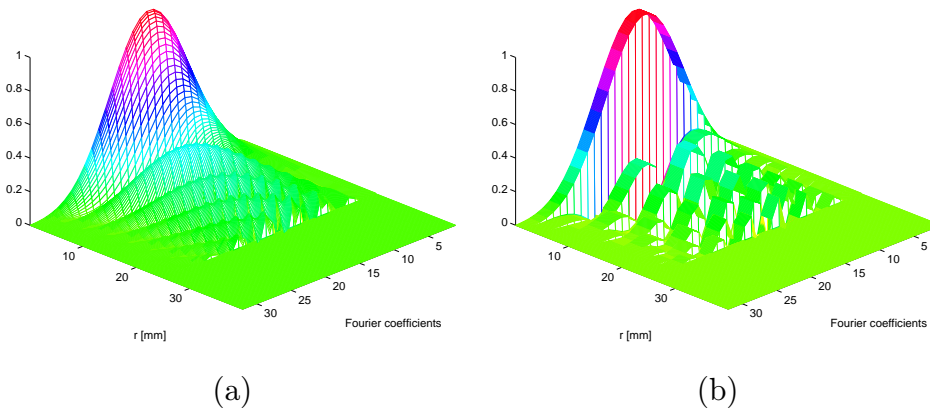
Figure 5.9: Initial field given to the SSC-algorithm for simulating the X wave in example 3 (a) exact aperture shading (b) aperture divided into 10 elements
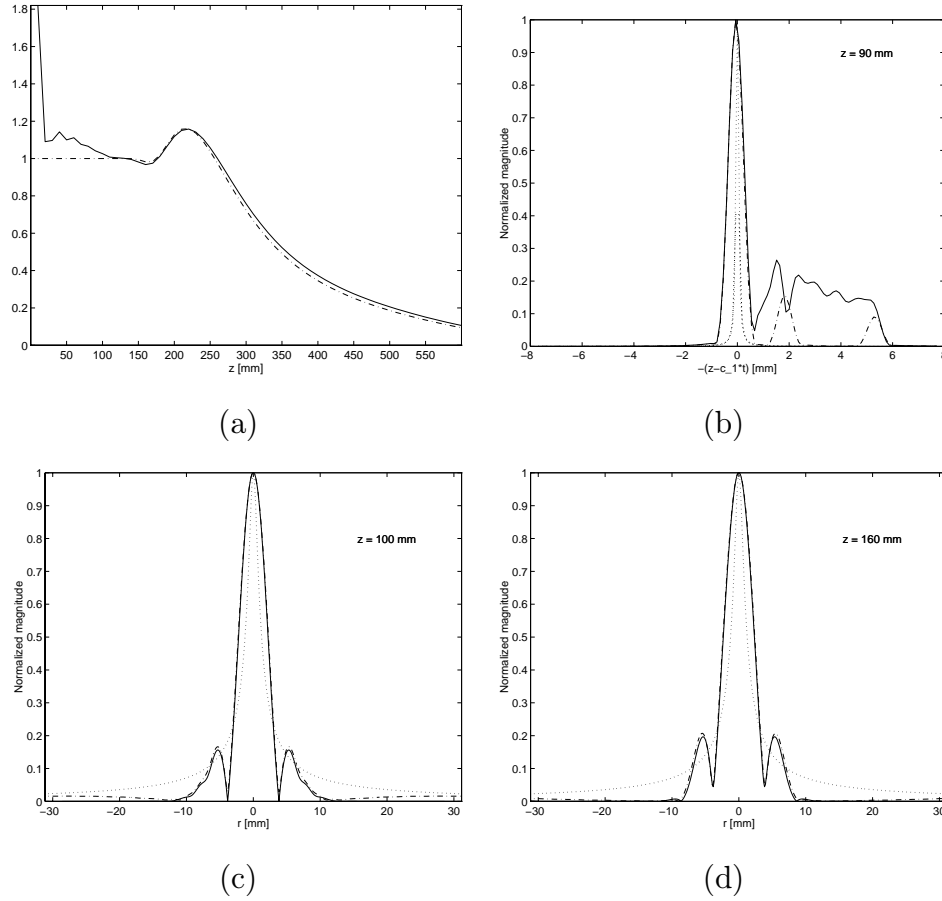
Figure 5.10: Simulations of the X wave in example 3. Parameters are $a_0 = 0.05$ mm and $\zeta = 4°$. Solid line represents finite element aperture, dash-dotted line represents exact aperture shading, and dotted line represents the exact X wave solution (a) Pulse peaks along the z-axis from $10 - 60$ mm. (b) Pulse along the time-axis at $z = 90$ mm. $z - c_1 t$ represents the distance away from the pulse center (c) Lateral beam profile at $z = 100$ mm (d) Lateral beam profile at $z = 160$ mm.
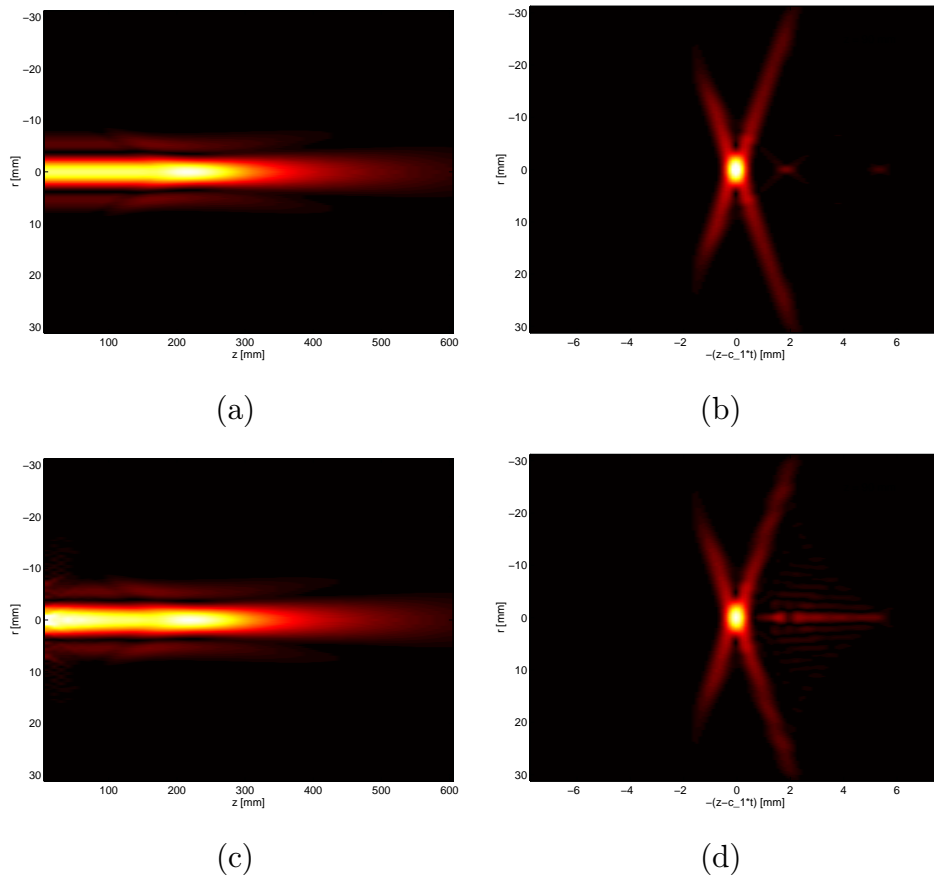
Figure 5.11: X wave in example 3 (a) Pulse peaks from $10 - 600$ mm with exact aperture shading (b) Pulse along the time-axis at $z = 90$ mm. (c) - (d) Corresponding results with the aperture divided into 10 annular elements.
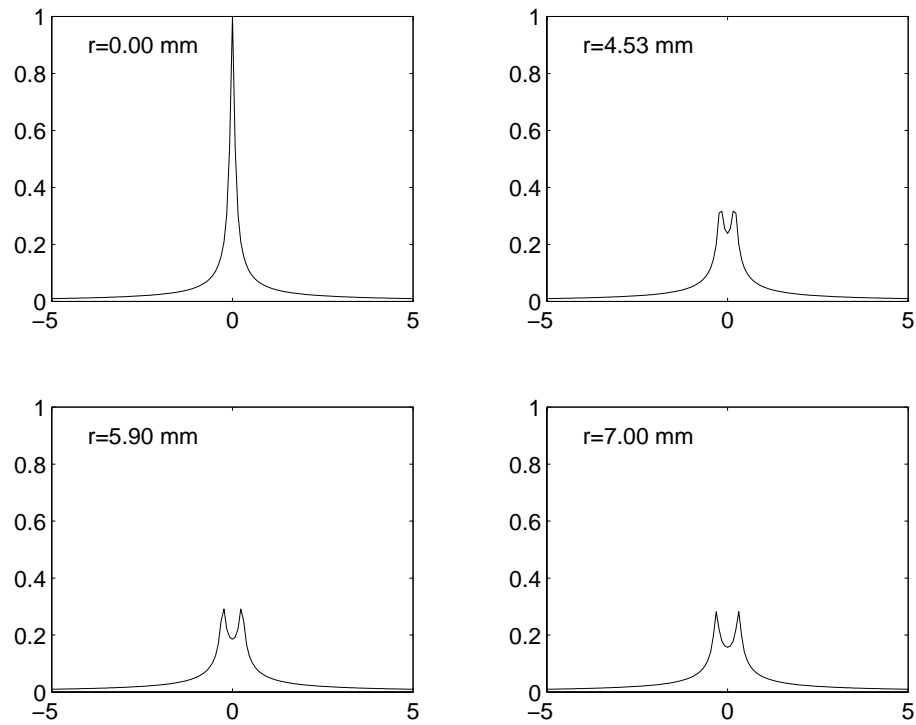
Figure 5.12: The pulses driven from each element of the annular array transducer in example 4. X-axis is time in microseconds. The given value, r, for each plot, is the average radius of each ring. This value is used when calculating the waveforms from eq. (5.15). The parameters a_0 and ζ are 0.05 mm and 2.57° respectively.
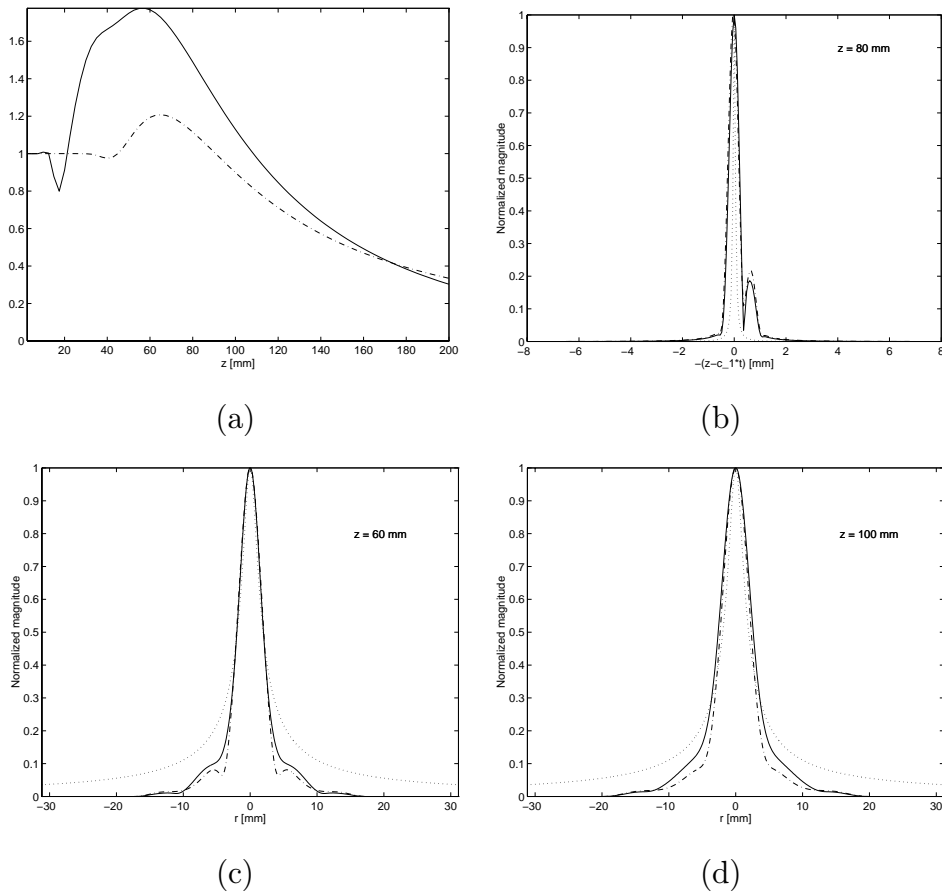
Figure 5.13: Simulations of the X wave in example 4. Parameters are $a_0 = 0.05$ mm and $\zeta = 4°$. Solid line represents finite element aperture, dash-dotted line represents exact aperture shading and dotted line represents the exact X wave solution (a) Pulse peaks along the z-axis from $10-200$ mm. (b) Pulse along the time-axis at $z = 80$ mm (c) Lateral beam profile at $z = 60$ mm (d) Lateral beam profile at $z = 100$ mm.
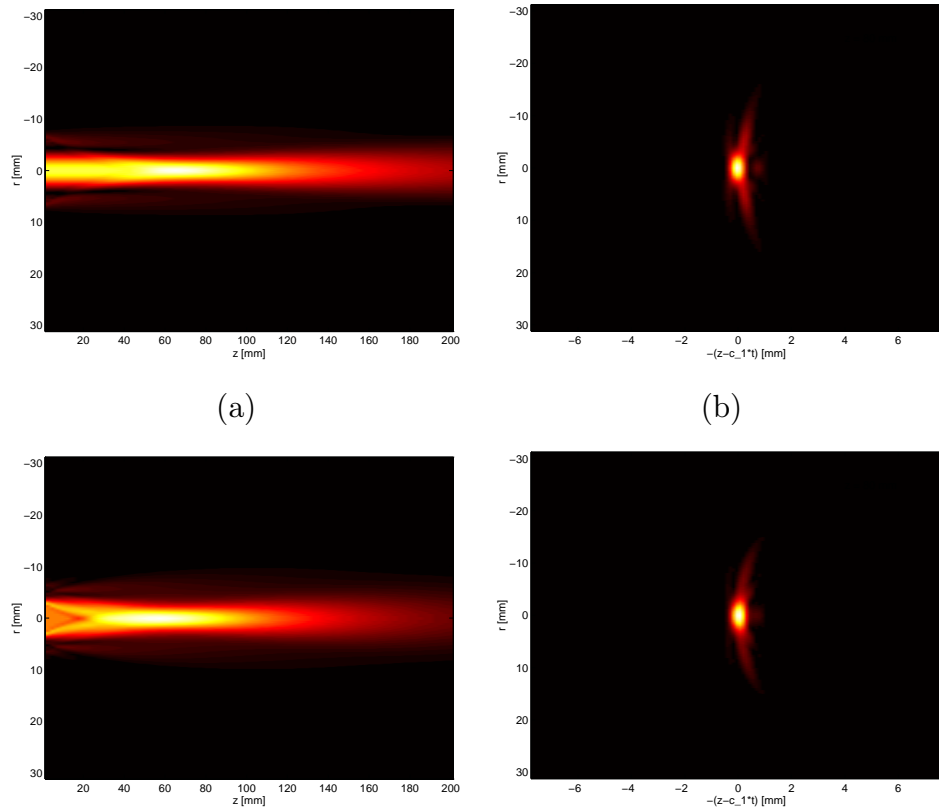
(a)   (b)

Figure 5.14: Image of the acoustic field generated by the transducer in example 4. (a) Peak of the pulse along the z-axis from 10-200 mm with exact aperture shading (b) The pulse along $z - c_1 t$ ($z = 80$ mm). $z - c_1 t$ is the distance away from the pulse center. (c)-(d) Corresponding results with finite element approximation.

Chapter 6

Nonlinear wave propagation

What we see from the derivation of the linear wave equation in chapter 3 is that it is a linear approximation to the relationship between pressure and density. In many applications this is a valid approximation. This assumption has been made in ultrasound imaging, and is valid for low initial pressure. The use of harmonics to enhance ultrasound images was in fact also based on this assumption. Introduction of contrast agents, which are microbubbles with nonlinear nature injected into the blood, was based on the assumption that sound propagation through tissue was linear, and that only the microbubbles in the blood would produce second harmonic signals. But with large amplitude signals excited from the transducer, harmonic generation is also present in propagation through tissue. The harmonics are generated as the beam propagates, so there is little energy in the second harmonic close to the source. But as the beam propagates, energy is transferred from the fundamental to higher harmonics, giving a second harmonic with a well formed beam profile.

6.1 Nonlinear wave equation

Retaining more than the first term in the Taylor expansion in (3.5) in the derivation of the linear wave equation, we get a nonlinear relationship between pressure and density. With $p - p_0 = p'$ describing the variations in the fluid caused by acoustic pressure and retaining two terms, (3.5) becomes [15]

$$p - p_0 = A \left(\frac{\rho - \rho_0}{\rho_0} \right) + \frac{B}{2} \left(\frac{\rho - \rho_0}{\rho_0} \right)^2 \tag{6.1}$$

where $A = \rho_0 c_0^2$ (the term involving specific entropy has been dropped, since we assume constant specific entropy). The effect of nonlinearity is dependent

Medium	$\beta = 1 + B/(2A)$
Fresh water	3.5
Sea water	3.6
Blood	4
Fat, human	5.8-6.2
Liver	4.34

Table 6.1: Nonlinearity parameter, β, for different media.

on the ratio, $B/(2A)$, where a larger ratio gives more nonlinear distortion in the medium. A common parameter to describe nonlinearity of a medium is

$$\beta = 1 + \frac{B}{2A} \tag{6.2}$$

β-values for different media are shown in table 6.1

We see from (6.1) that the nonlinear effects are somehow proportional to the linear, depending on β, but squared. This leads us to believe that higher harmonics generated by nonlinear propagation would have better sidelobe structure than the fundamental. What should also be noted, is that since the relation is no longer linear, different initial pressure would not just lead to a different scaled solution, but the generation of higher harmonics is in fact dependent on the pressure of the transducer.

The derivation of the general nonlinear wave equation is rather complicated and is outside the scope of this thesis. This equation is given by [16]

$$\frac{\partial^2 p}{\partial t^2} - c_0^2 \nabla p = \frac{\partial}{\partial t^2} \left[(\nabla p)^2 + \frac{B/A}{2c_0^2} \left(\frac{\partial p}{\partial t} \right)^2 + b \nabla p \right] \tag{6.3}$$

Here b is known as the absorption coefficient given by

$$b = \frac{1}{\rho_0} \left(\zeta + \frac{4}{3} \eta + \left(\frac{1}{c_v} - \frac{1}{c_p} \right) \kappa \right) \tag{6.4}$$

where η and ζ are shear and bulk viscosities, κ is the coefficient of thermal conductivity, and c_p and c_v are the specific heats. The simulations of acoustic fields under nonlinear conditions done here, are not based on this equation, but use a model equation to predict the nonlinear effects. Since solving
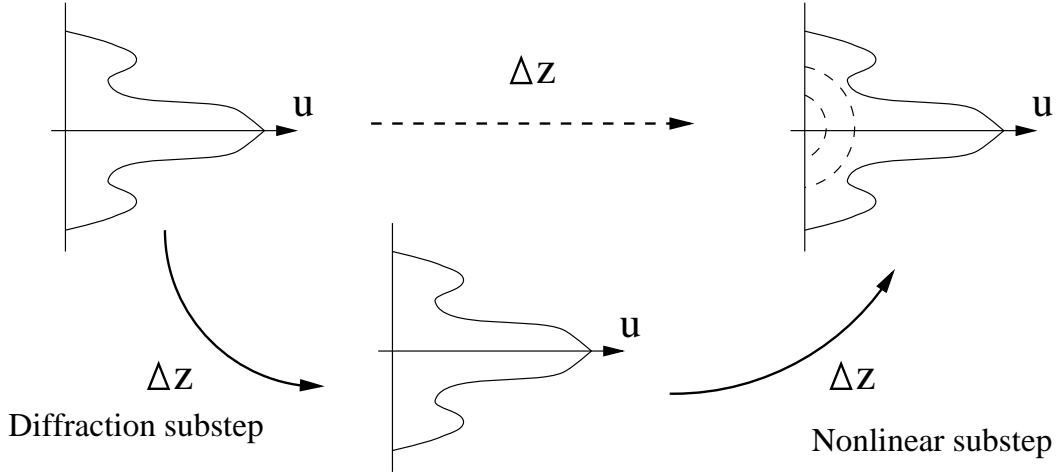
Figure 6.1: Illustration of the algorithm for propagating a normal velocity field a distance, Δz, under nonlinear conditions, using two substeps.

(6.3) numerically might be impossible, a number of model equations have arisen, being valid under certain simplified conditions. Most of them assumes that nonlinear distortion is small on the wavelength scale, meaning that the wave is locally plane and linear. The model equation which the simulation algorithm presented next is based on, is the Burgers equation. It is given by

$$\frac{\partial p}{\partial z} - \frac{\epsilon}{\rho_0 c_0^3}(p - p_0)\frac{\partial p}{\partial \tau} - \frac{b}{2c_0^3}\frac{\partial p}{\partial \tau^2} = 0 \tag{6.5}$$

where $\tau = t - z/c_0$ and $\epsilon = (\gamma + 1)/2$, and γ is given by

$$\gamma = \frac{B}{A} + 1 \tag{6.6}$$

6.2 Simulation of nonlinear wave propagation

The method used for simulating wave propagation under nonlinear conditions is based on the RFSC algorithm described in section 3.3.6 in chapter 3. It is a multistep quasilinear method that solves the Burgers equation in the frequency domain by propagating a number of harmonics stepwise along the z-axis [17]. The algorithm involves two substeps for propagating the field one step along the axial direction, a linear substep that acounts for diffraction and a nonlinear substep that accounts for the generation of higher harmonics. The linear substep propagates the field between to planes with a small distance

Δz as described by the RFSC algorithm. The multistep approach, which also could be used in linear propagation, means that after the first substep the source is no longer of finite extent. The source of the next substep is then the lateral field distribution at $z + \Delta z$ which in theory is infinite but has small amplitude when the radius increases.

The nonlinear substep supplements the linear substep by adding nonlinear effects to the diffracted field. If the propagating field was a plane wave travelling in the z-direction, nonlinear effects could be computed using the frequency domain solution to the Burgers equation for small steps, Δz. In our application the field is not a plane wave so the nonlinear step is added to linear, so both nonlinearity and diffraction is accounted for.

The input to the algorithm is a multiharmonic field, but if simulating continuous wave excitation of the tranducer, only the first harmonic is different from zero in the first step. Energy in the other harmonics are generated by nonlinearity in the medium, and these effects are added as the wave propagates. The nonlinear step can be written as

$$
\begin{aligned}
u_n(z + \Delta z, i) = \quad & u'_n(z + \Delta z, i) + j\frac{\beta \pi f \Delta z}{2c^2}\left(\sum_{k=1}^{N-1} ku'_k u'_{n-k}\right. \\
& \left. + \sum_{k=n}^{N} nu'_k u'^{*}_{k-n}\right), n = 1, 2, .., N
\end{aligned}
\tag{6.7}
$$

where $u'_n(z + \Delta z, i)$ denotes the field after the linear substep, * denotes complex conjugation, f is the fundamental frequency, u_n is then nth harmonic in an N term Fourier series, and i denotes the ith lateral field sample. The first summation in (6.7) represents the gradual buildup of the nth harmonic by nonlinear combination of other harmonics that have have a sum frequency of nf. The second summation is the transfer of energy from the nth harmonic to other harmonics, with a difference frequency of nf. The complete algorithm then becomes

1. Choose spatial transform extent, spatial sampling rate, stepsize Δz and the number of harmonics to include in the simulation.

2. Sample the source function spatially for each harmonic. For continuous wave excitation only the first harmonic is sampled. Call the sampled source function u'_n, where n denotes the nth harmonic.

3. Sample the analytic Hankel transform of the normal velocity point spread function for all harmonics to obtain $\hat{H}_n(\Delta z, R)$, where Δz is a small propagation distance. (Apply the ray theory truncation to the analytic Hankel transform).

4. Propagate the field a distance Δz by multiplying the Hankel transform of the source function, u'_n, and the point spread function $\hat{H}_n$, for each harmonic and then doing the inverse Hankel transform. Call the resulting field $u'_n(z + \Delta z, i)$ (where $z = 0$ in the first step).

5. Add nonlinear effects by inserting $u'_n(z + \Delta z, i)$ in (6.7).

6. Repeat step 4 and 5 until you reach the final propagation distance. Between each iteration, $\hat{H}_n(\Delta z, R)$ is truncated, according to ray theory.

The values, u_n, are now the lateral field samples at distance $m \times \Delta z$, where m is the number of steps, and n is the nth harmonic.

6.3   Nonlinear wave propagation

Since a transducer has limited bandwidth, the transmitted frequency in harmonic imaging must be lower than the central frequency of the transducer. The transmitted frequency is typically about 60 % of the central, and reception is done at twice this frequency. This gives a broader transmitted beam, but penetration is deeper because lower frequencies are less attenuated when propagating through tissue. As the transmitted beam propagates, it generates energy at higher harmonics, so reception is done on the second harmonic, or twice the transmitted frequency. The second harmonic is narrower and has lower sidelobes than the first harmonic, giving images with better contrast and resolution.

As nonlinear distortion is dependent on the initial pressure of the transducer, as high pressure on the transducer surface as possible is desirable, as this gives more second harmonic energy. The pressure in ultrasound imaging is limited though, as high amplitude signals could cause damage to the tissue. The pressure in ultrasound imaging is measured in mechanical index (MI), which is given by [18]

$$\text{MI} = \frac{p^-}{\sqrt{f_0}} \tag{6.8}$$

where p^- denotes maximum negative pressure amplitude, and f_0 is the center frequency in MHz. For safety reasons, this value must be less than 1.9. The maximum pressure, p^-_{max}, is found by finding the maximum pressure in a medium with 0.3 dB/MHz/cm attenuation. Since there is not just a single frequency in imaging with pulsed excitation and there is energy at higher harmonics in harmonic imaging, the frequency, f_0, must be estimated. In the following results, calculation of the MI value has been simplified to finding the

<center>(a)   (b)</center>
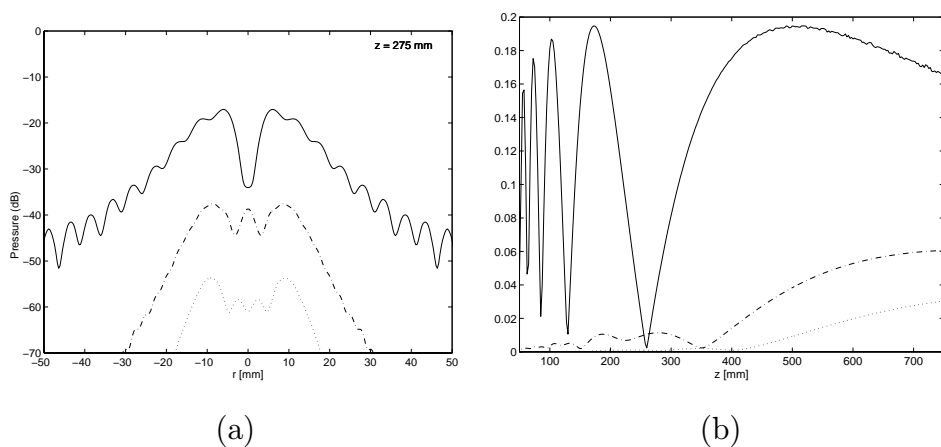
Figure 6.2: First three harmonics of an unfocused 2.25 MHz piston transducer
(a) lateral pressure field at $z = 275$ mm (b) axial amplitude

maximum value of the first harmonic, with f_0 as the transmitted frequency.
All results are within MI < 1.9.

Christopher *et. al* [17] have simulated an unfocused, circular piston trans-
ducer with radius 19 mm, operating in water at 2.25 MHz. The initial am-
plitude was 100 kPa, and the simulated results were compared to experi-
mentally obtained data. Figure 6.2 (a) shows the lateral field distribution of
the first three harmonics at $z = 275$ mm and figure 6.2 (b) shows the axial
pressure from $z = 50 - 750$ mm, computed by the implementation done in
this thesis. No attenuation has been included here. This implementation
shows differences in amplitude of the second and third harmonics compared
to Christopher's results, where those harmonics are higher. Wave or phase
front curvature has not been accounted for in the nonlinear step, as suggested
in the referred article. To better account for wave or phase front curvature,
correction terms are added where Δz is replaced by $\Delta z / \cos \theta[u_1(z,i)]$, and
$u_n(z,i)$ is replaced by $u_n(z,i) / \cos \theta[u_1(z,i)]$, where $\theta[u_1(z,i)]$ is given by

$$\theta[u_1(z,i)] = \frac{d}{dr}\left[\tan^{-1}\left(\frac{\mathrm{Im}[u_1(z,r)]}{\mathrm{Re}[u_1(z,r)]} \right) \right]_{r=r_i} \tag{6.9}$$

This is done to account for direction and magnitude of the actual, not normal,
field. Also note that the relation (3.63), which converts normal velocity to
acoustic pressure, is inaccurate in describing the near-field of the unfocused
piston source. The lateral distribution in figure 6.2 (b) is practically identical
with the results of Christopher *et. al*, although the amplitude of the second
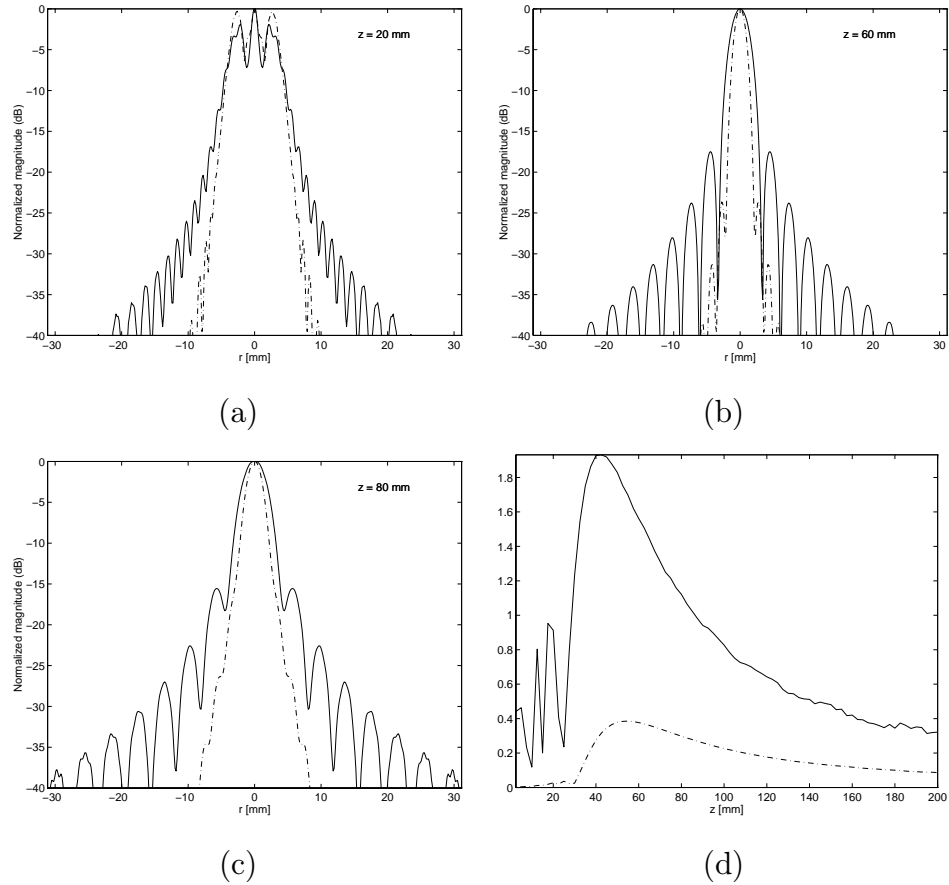and third harmonic is lower.

Figure 6.3: Lateral beamprofile for the first (solid) and second (dotted) harmonic when transmitting at 2.275 MHz with initial pressure of 4 kPa. The transducer is focused at 60 mm. (a), (b), (c) Lateral fields at $z = 20$, 60 and 80 mm (normalized and dB scaled) (d) Pressure along the direction of propagation, $z = 10 - 200$ mm, y-axis is pressure (MPa).

Figure 6.3 (a)-(c) shows simulations of a spherically focused beam at different distances. The transducer has a diameter of 15 mm and is focused at 60 mm. The transmitting frequency is 2.275 MHz, so this transducer could have a central frequency of 3.5 MHz. Figure 6.3 (b) shows the lateral field at the focusing point, $z = 60$ mm, for the first and second harmonic. At this distance the beamprofile is optimal, and we see that the beam is narrow and the sidelobes are low for both harmonics. Note that the plots have been scaled according to their maximum value. The second harmonic is much lower, as shown in figure 6.3 (d). We see that the second harmonic is narrower and has lower sidelobes than the first. Also note the extra sidelobes, referred to as fingers. Figure 6.4 (a) and (b) shows the beamprofile for the first and second harmonic from $z = 2 - 200$ mm. We see that there is a small, optimal focusing area around the focusing point for both harmonics. The second harmonic is low before the focusing point, due to the broad first harmonic in the same area.

6.4   Nonlinear propagation of limited diffraction beams

Simulations of the unfocused piston and spherically focused beams show that the second harmonic is narrower and has lower sidelobes than the fundamental. Applying nonlinear propagation conditions to the Bessel beam and X waves, the high sidelobe level is expected to decrease on the second harmonic, while still having an approximate depth-independent focus through the depth of field. The second harmonic of the spherically focused beam is small before the focusing point, but has good focusing properties within the area of focus. The small second harmonic close to the transducer is due to the broad first harmonic before the focusing point. We know that the second harmonic is generated from the first as the beam propagates, and since the energy is broadly distributed, there is little generation of second harmonic energy. The limited diffraction beams have an approximately depth independent shape, so the beam is narrow through the entire depth of field. This gives second harmonic energy close to the source also.

Figure 6.5 and 6.6 show simulations of the first and second harmonic of a Bessel beam with the same transducer as in the previous section, with exact aperture shading. The Bessel shading is chosen to include one sidelobe of the Bessel-function, giving $\alpha = 736$. This configuration gives a depth of field of 95 mm. From figure 6.5 (d) we see that there is energy in the second harmonic almost through the entire depth of field, as opposed to the

spherically focused beam which has mainly second harmonic energy from the focusing point. This is also seen in figure 6.6 (b).

But the lateral plots in figure 6.5 (c) show an unexpected effect. Although the second harmonic is slightly narrower than the first, the first sidelobes are extremely large, in great contrast to the spherically focused beam. The large first sidelobes are probably caused by diffraction of the second harmonic, since the second harmonic is both large and narrow at an early stage and diffraction of the second harmonic is added to the generated second harmonic as the beam propagates. From figures 6.5 (a)-(c) it is seen that the high sidelobes are generated as the beam propagates, and seems to be so-called fingers or extra sidelobes. From the figures it seems reasonable that the extra sidelobes are caused by diffraction. The large second harmonic close to the source is not necessarily desirable, because patients with inhomogeneous skin layers would cause the beam to diffract when propagating into the body. The spherically focused beam has therefore good second harmonic properties, and is still optimal within the focusing area. But the focusing area is rather small, and the beam profile is far from optimal when moving far away from the focusing point.

Figure 6.7 shows another nonlinear simulation of the first and second harmonic of the Bessel beam. Simulation is done with the same transducer, but with $\alpha = 641$ as in example 2 in chapter 5. We see that there is a growth of extra sidelobes as the beam propagates, which become large at $z = 90$ mm. The growth of extra sidelobes is not as evident as the previous example, due to a broader beam because of the smaller α.

One might think that the unexpected sidelobes of the Bessel beam's second harmonic is a result of the equal weighting of each frequency of the Bessel beam, so the second harmonic has different focusing. Then we would expect different results from the X waves, where each frequency is focused in the same area. Since the X wave is a broadband pulse, simulation is done by transmitting on a band around $0.65 f_c$, where f_c is the centeral frequency of the transducer. The second harmonic is found by calculating the pulse at the corresponding band at $1.3 f_c$. Figure 6.8 and 6.9 show simulations of an X wave with the same depth of field as the Bessel beam with $\alpha = 736$. We see from figures 6.8 (a)-(c) that the same effect regarding sidelobes of the second harmonic is present, and figure 6.9 (d) shows that there is still a great amount of energy in the X branches. One must remember that the second harmonic is not produced by transmission of second harmonic energy, so no focusing of the doubled frequency has taken place. The sidelobes of the second harmonic are produced as the beam propagates, and since both the Bessel beam and X wave are narrow and large from the source through the depth of field, generation of higher harmonics is similar.

A larger limited diffraction transducer with more lobes of the Bessel function included, would however give better second harmonic properties because of less diffraction. A Bessel beam with a corresponding transducer as example 1 in chapter 5 (50 mm transducer with ten lobes of the Bessel function included) is simulated in figure 6.10 and shows better sidelobe structure at the end of the depth of field. Transmit is done at 65% of the central frequency of 2.5 MHz, which gives a theoretical depth of field of 130 mm. The second harmonic is narrower and the sidelobes are lower than for the fundamental frequency. Still, the sidelobes are high. As mentioned earlier, this transducer is very large so the previous examples are of more practical interest.

6.5 Modifying the limited diffraction beams

The question is how to give the limited diffraction beams' second harmonic properties similar to the spherically focused, while maintaining a large depth of field. A large depth of field would be at cost of large sidelobes, but at least the second harmonic sidelobes should be lower than for the first. Based on the assumption that the large second harmonic sidelobes are caused by diffraction, generation of second harmonic energy further away from the transducer surface would be desirable. For limited diffraction beams, this means that the first harmonic must be low near the transducer. To obtain this, we take a look at the Axicon transducer. If the top is cut off as in figure 6.11, we get a theoretical focusing area which extends from where the lines perpendicular to the start of the transducer intersect, to where the lines perpendicular to the cone edges intersect. As an analog to the Bessel beam and X wave, it means setting part of the aperture weighting to zero, for example by not transmitting any signal from the inner element of an annular array transducer. Theoretically this gives no first harmonic before the start of the focusing area given by

$$\text{SOF} = \frac{R_h}{\tan \zeta} \tag{6.10}$$

where R_h is the radius of the hole, and ζ is the Axicon angle (or ϕ given by (4.22) for the Bessel beam). Because of diffraction there is energy at closer distances, but it gives a second harmonic with the desirable properties. Figure 6.12 shows the aperture weighting of a modified Bessel beam where $\alpha = 736$. The mainlobe of the Bessel-function, $J_0(\alpha r)$, which gives the exact aperture shading of the original Bessel beam, has been set to zero. The theoretical focusing area is given by

$$\text{SOF}_{MB_0} = \frac{3.3 \text{ mm}}{\tan \phi} = 41 \text{ mm} \tag{6.11}$$

and

$$\mathrm{DOF}_{MB_0} = \frac{7.5 \text{ mm}}{\tan \phi} = 95 \text{ mm} \tag{6.12}$$

Figure 6.13 (a) and (b) shows the first and second harmonic of the modified Bessel beam. The focusing area of the first harmonic is about what is predicted by theory. Note that the effective aperture has been reduced from 15 mm to 8.4 mm, and the aperture shading is no longer a limited diffraction solution of the wave equation, which is the reason why the beam seems to diffract through the depth of field. But it is the second harmonic that is of interest, and figure 6.13 (b) shows that it has some of the desirable properties. Second harmonic energy is low near the transducer, and the depth of field is large. Figure 6.14 shows a comparison of the spherically focused beam and the modified Bessel beam. Diffraction of the second harmonic no longer causes extremely large sidelobes of the modified Bessel beam, and where the spherically focused beam gets broader, the modified Bessel beam stays relatively narrow, though at cost of large sidelobes.

Figure 6.15 and figure 6.16 show a modified X wave with parameters corresponding to the modified Bessel beam. Again note that Bessel and X wave results are not comparable, because of the continuous wave Bessel excitation. The lateral plots in figure 6.15 (a)-(c) shows that both the first and second harmonic gets broader as the beam propagates, similar to the Bessel beam. The modified beams would not be termed limited diffraction beams, since the focus is no longer equal in each transverse plane along the direction of propagation. Still, the modified X wave represents a non-dispersive, supersonic wave. The pulse peaks at time, $t_0 = z_0 cos(\zeta)/c$, which is seen in figure 6.16 (b) and (d) where the center of the plots is at time t_0. This shows that the X waves are mainly composed of energy at the edges of the transducer at large distances. From figure 6.16 (b) we see that the modified X wave still has energy in the X branches, but for the second harmonic in figure 6.16 (d) it has been greatly reduced.

At the end of my work on this thesis, I found that Lu *et. al*[19] have had a similar idea of deleting the center of the Bessel function, but with a different motivation. Their goal was to avoid skin heating as a result of the large amplitude center of the Bessel beam, and shows from computer simulations that when deleting up to three elements of a Bessel transducer, the differences from using all elements are negligible after distance $z/D \geq 1.0$, where D is the diameter of the transducer . They do however use a larger transducer including more Bessel lobes so the effective aperture size is not reduced to same degree as in my simulations, resulting in a more uniform beam.

Not transmitting any signal from a large part of the center of the transducer can be compared to using a ring transducer for transmission. A ring transducer is just a thin ring radiating energy, giving a large depth of field [3]. Near the source the lateral field has no central maximum, but in the far-field there is a maximum value at the center and the lateral distribution is proportional to the Fourier transform of the transducer aperture. The beamwidth increases monotonically with distance, which is also seen for the modified limited diffraction beams. The difference between the beams generated by a ring transducer and the modified limited diffraction beams, is that a larger aperture is used for the modified limited diffraction beams, and aperture weighting is included.
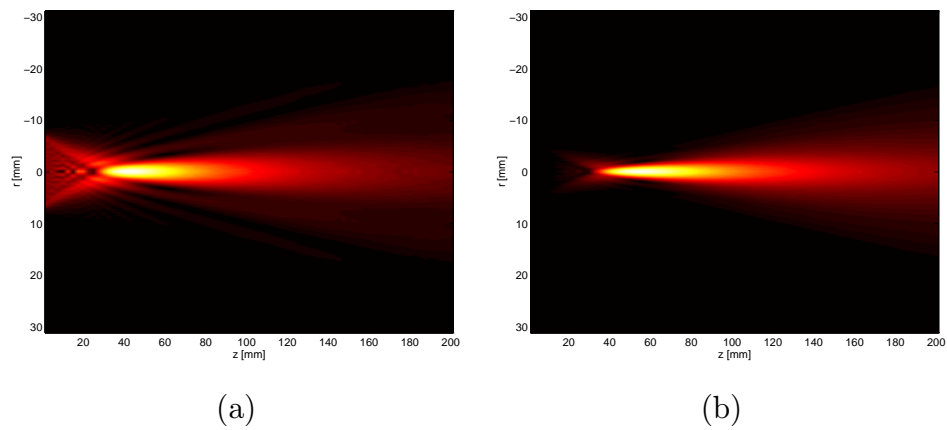
Figure 6.4: Spherically focused beam. The plots are normalized according to the maximum value of the respective harmonic (a) first harmonic (b) second harmonic. Both harmonics give a small, optimal focusing area.
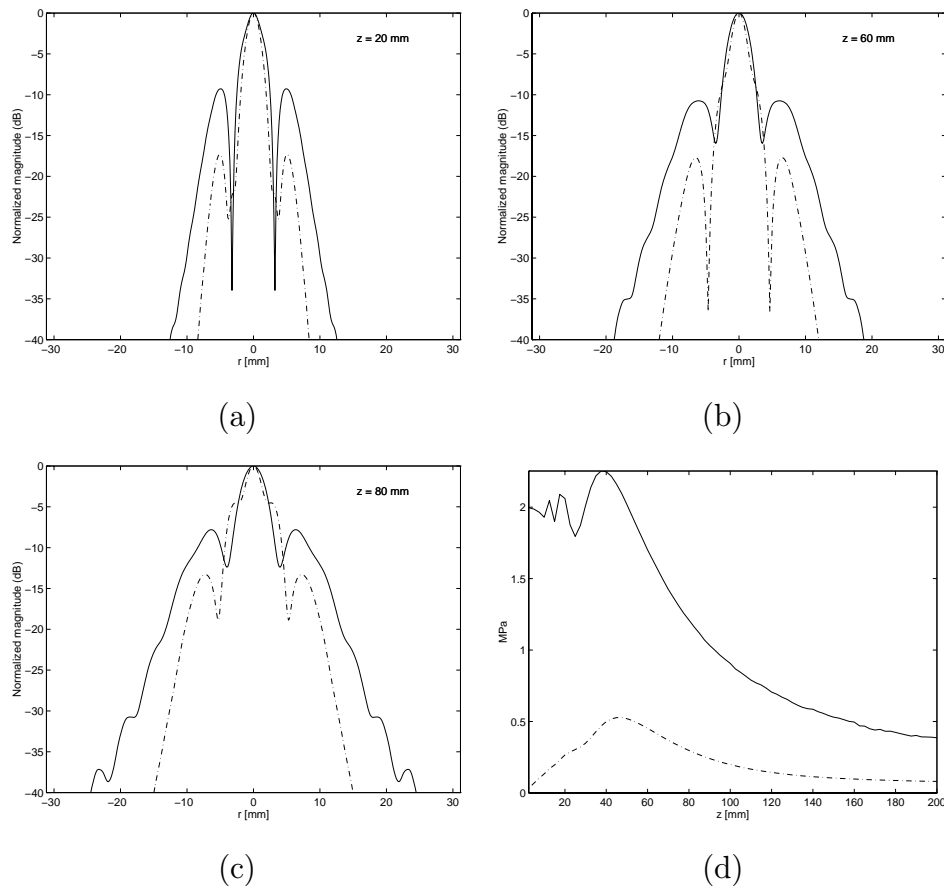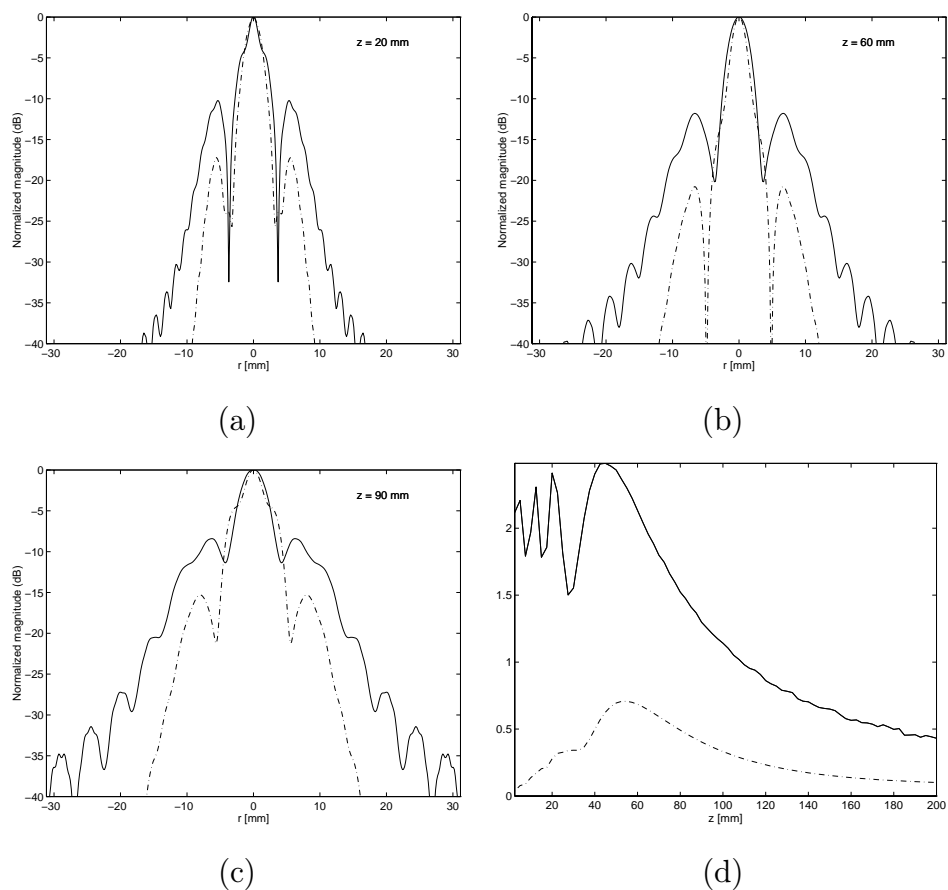
(a)

(b)

(c)

(d)

Figure 6.5: First (solid) and second (dotted) harmonic of the Bessel beam with $\alpha = 736$ m^{-1}. (a), (b) and (c) Normalized lateral plots (dB) at $z = 20$, 60, and 80 mm respectively (d) Pressure distribution along the direction of propagation for the first and second harmonic, y-axis is pressure (MPa)

(a)   (b)
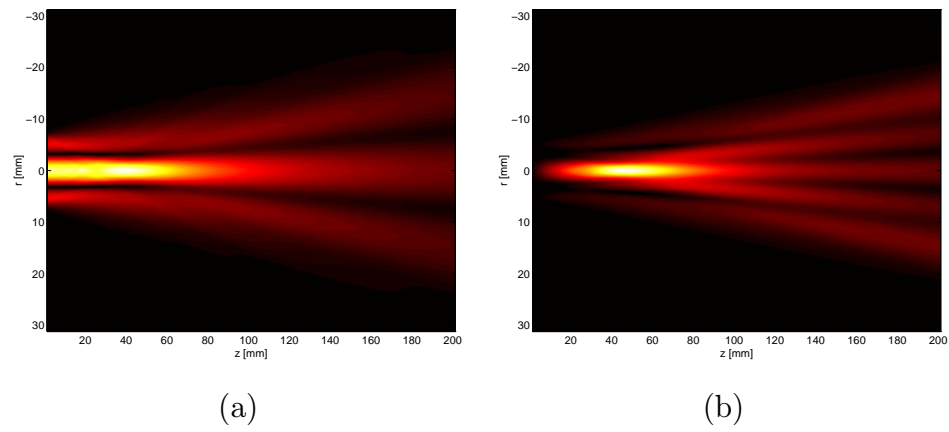
Figure 6.6: First and second harmonic of the Bessel beam with $\alpha = 736 \text{ m}^{-1}$ (a) first harmonic (b) second harmonic

Figure 6.7: First (solid) and second (dotted) harmonic of the Bessel beam with $\alpha = 641$ m^{-1}. (a), (b) and (c) Normalized lateral plots (dB) at $z = 20$, 60, and 90 mm respectively (d) Pressure distribution along the direction of propagation for the first and second harmonic, y-axis is pressure (MPa)
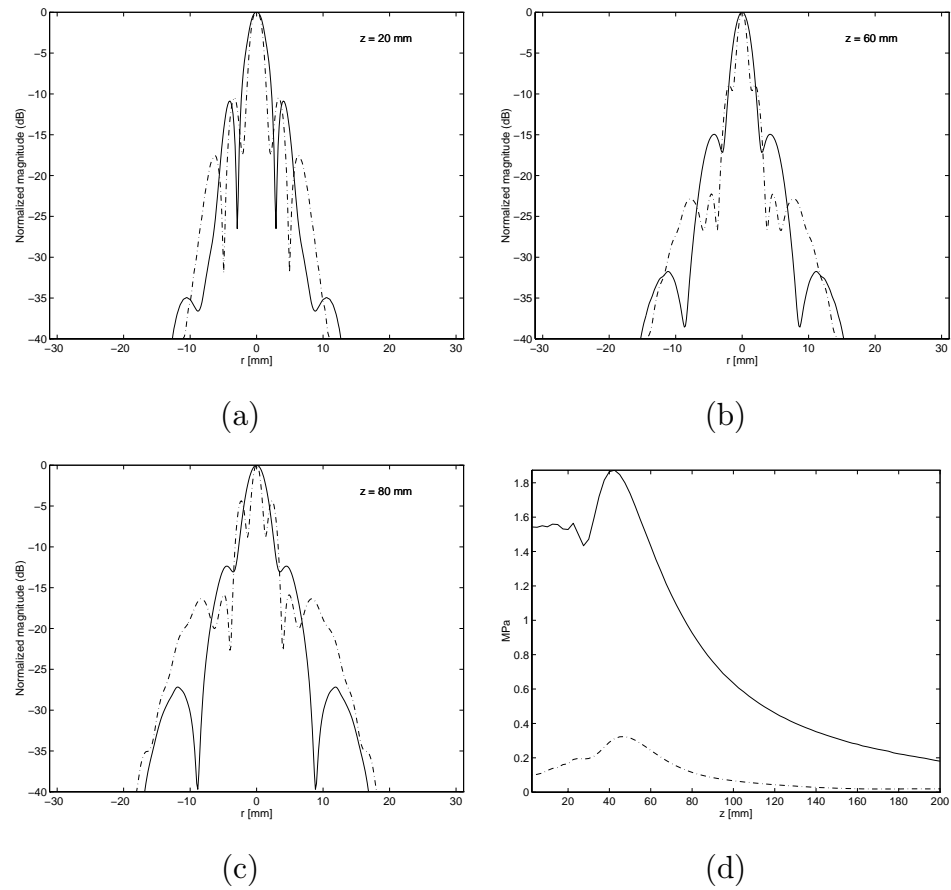
(a)

(b)

(c)

(d)

Figure 6.8: First (solid line) and second harmonic (dotted line) of X wave with parameter $a_0 = 0.05$ mm and $\zeta = 4.54°$. (a)-(c) Lateral field at $z = 20$, 60 and 80 mm. (d) Pulse peaks from $z = 20 - 200$ mm
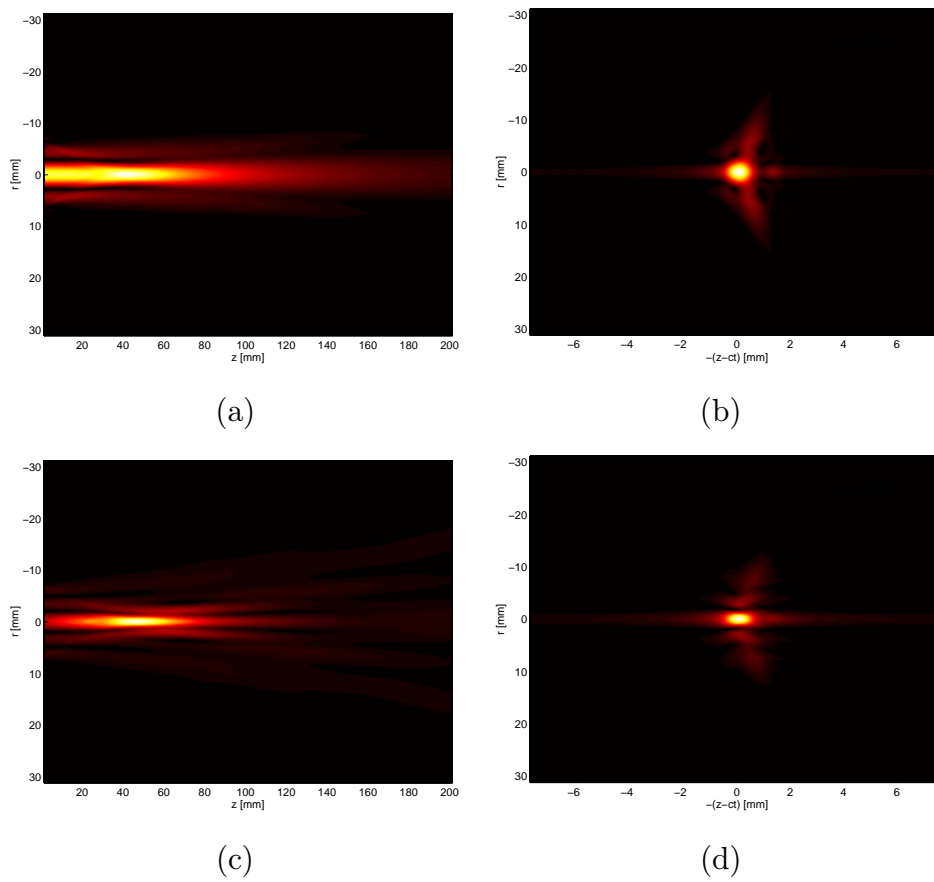
(a)

(b)

(c)

(d)

Figure 6.9: Images of X wave (a) Pulse peaks from $z = 20 - 200$ mm (b) Pulse at $z = 60$ mm (c)-(d) Corresponding images for the second harmonic
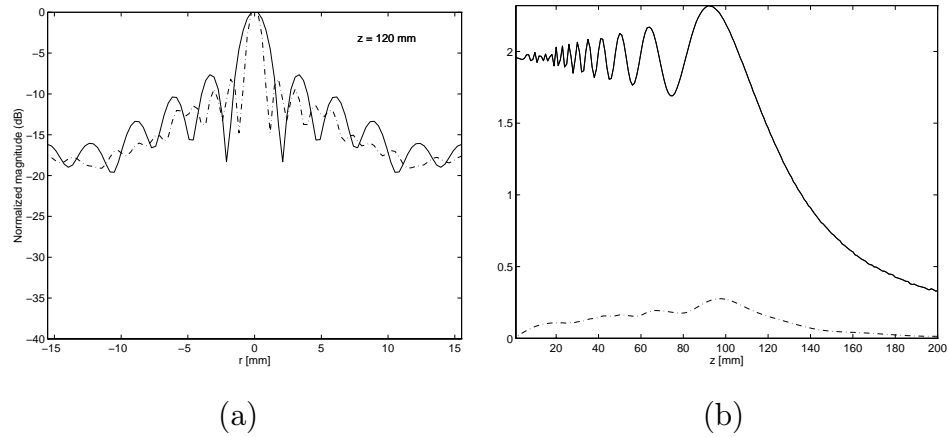
Figure 6.10: First and second harmonic of Bessel beam produced by a 50 mm transducer with exact aperture shading. Solid line represents the first harmonic and dotted line is the second harmonic (a) Lateral field at $z = 120$ mm (b) Axial amplitude
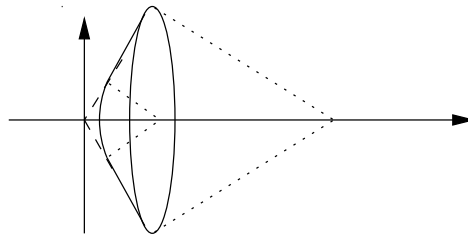

Figure 6.11: Axicon transducer with the top cut off. This gives an area of focus which starts beyond the transducer surface.
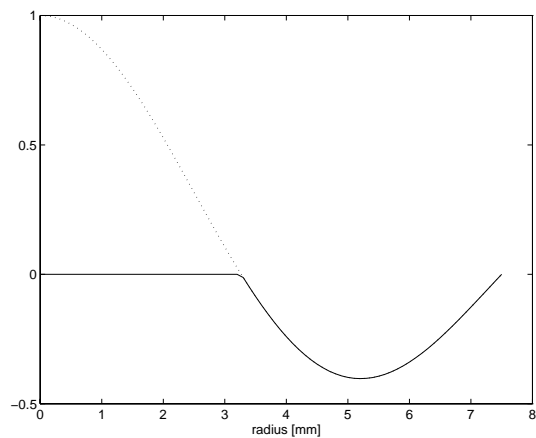
Figure 6.12: Exact aperture shading of the modified Bessel beam. The main-lobe of the Bessel function has been set to zero, giving a focusing area which starts beyond the transducer surface.
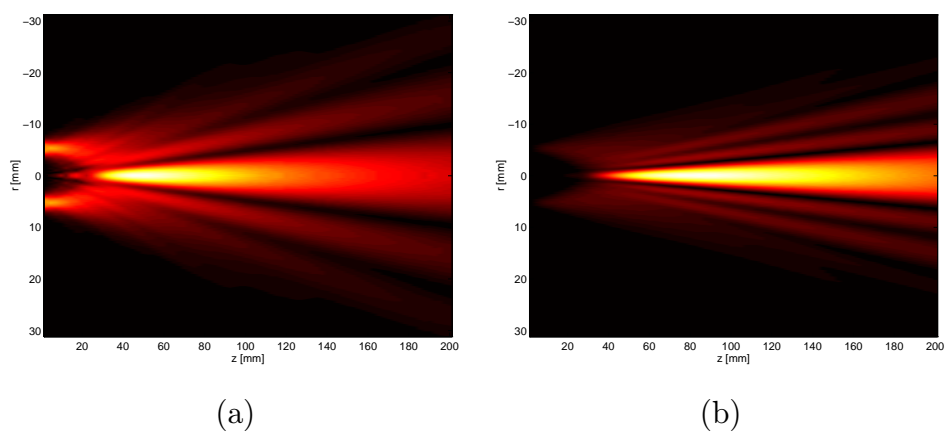

(a)   (b)

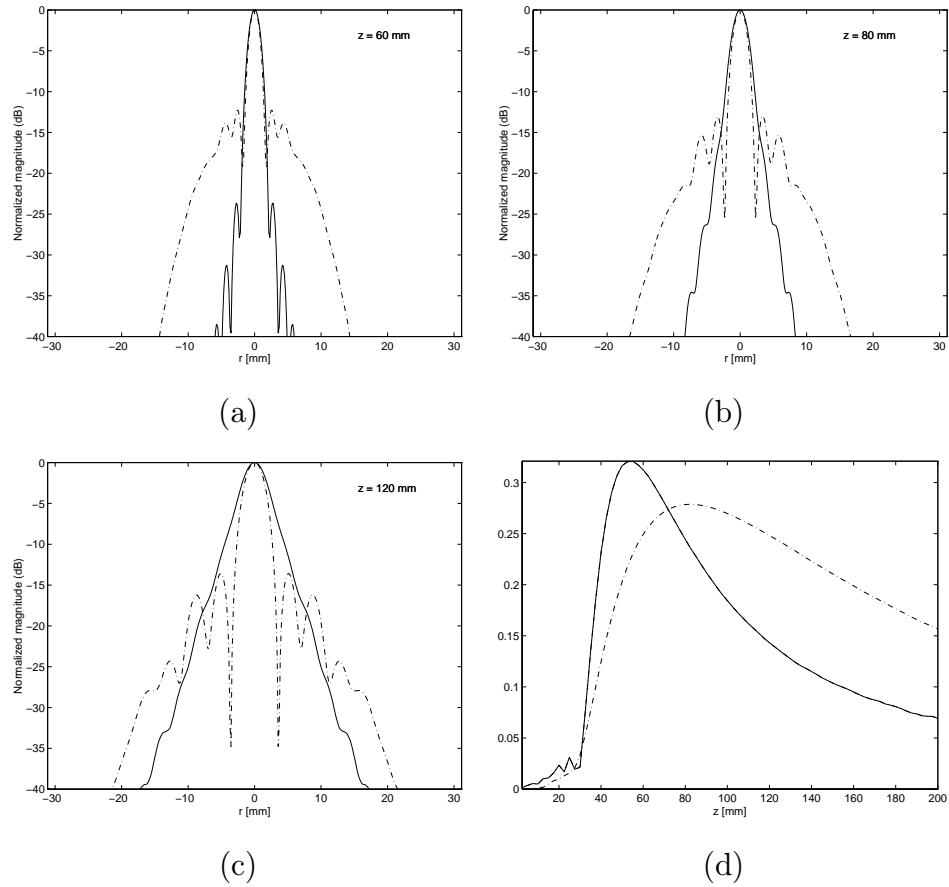Figure 6.13: (a)-(b) First and second harmonic of modified Bessel beam

Figure 6.14: Comparison of the second harmonic of the spherically focused (solid line) and modified Bessel beam (dotted line) (a), (b) and (c) lateral plots (dB) at $z = 60$, 80 and 120 mm (d) pressure of the second harmonic along the direction of propagation

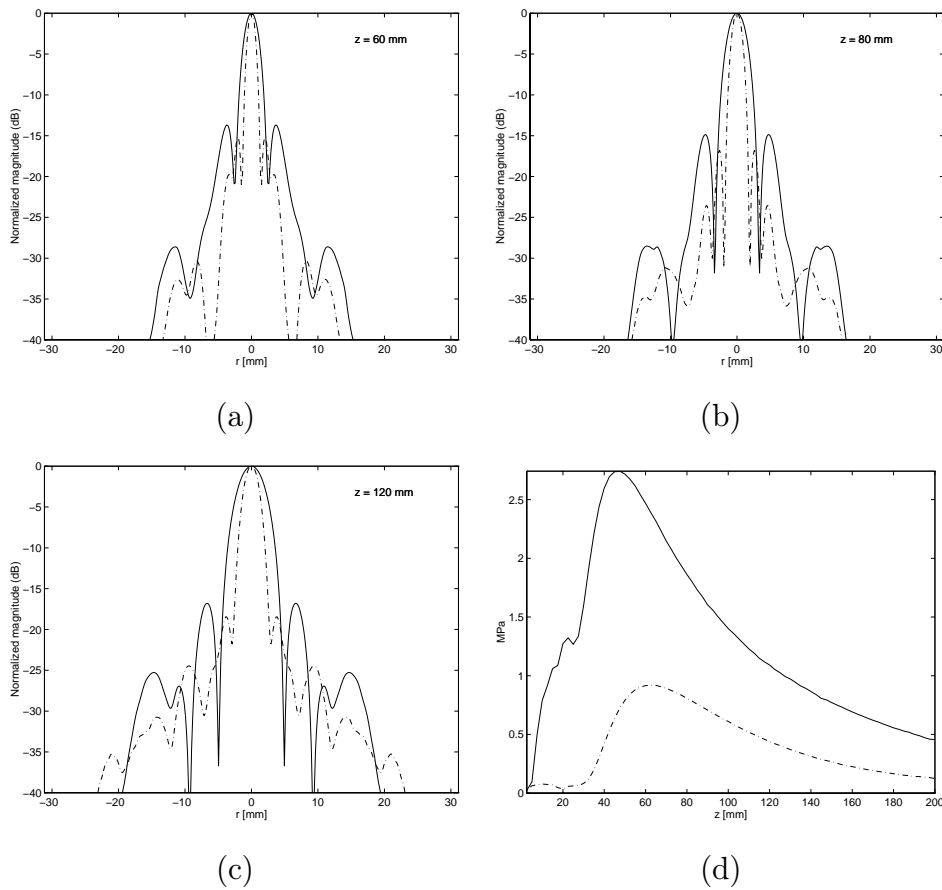Figure 6.15: First (solid line) and second harmonic (dotted line) of modified X wave (a)-(c) Lateral field distribution (dB) at $z = 60$, 80 and 120 mm (d) Pulse peaks along the direction of propagation
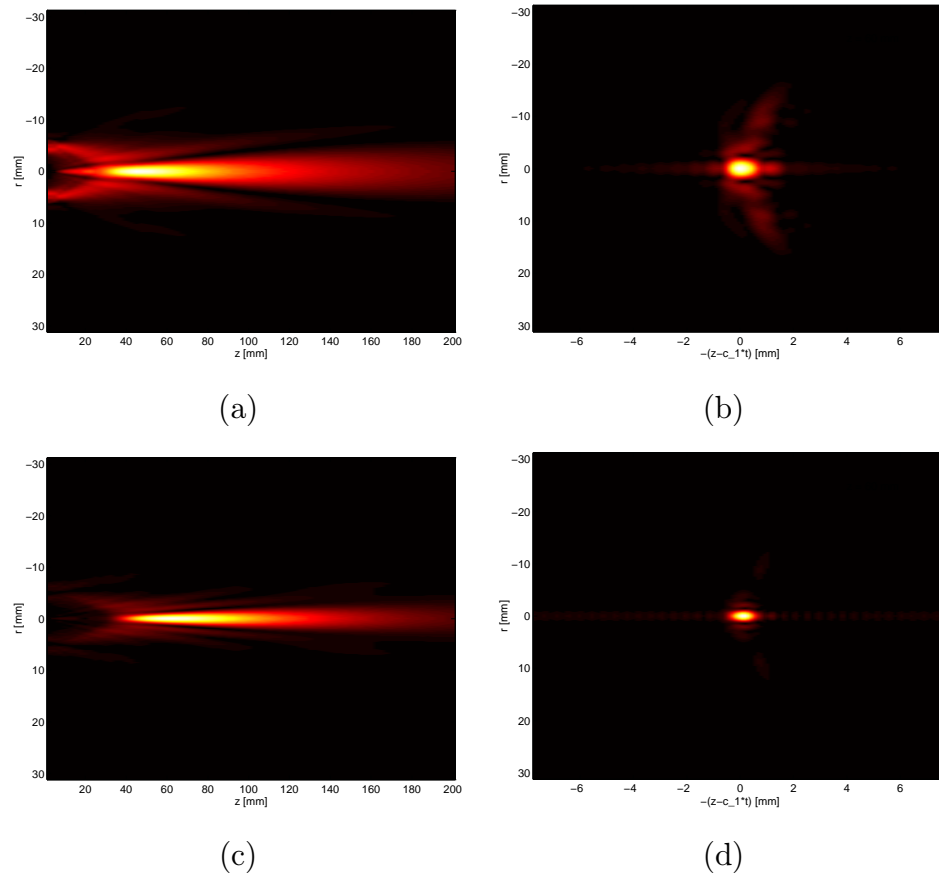
Figure 6.16: (a) Pulse peaks of the first harmonic of the modified X wave, from $z = 2 - 200$ mm (b) Pulse of the first harmonic of the modified X wave at $z = 60$ mm (c)-(d) Corresponding images of the second harmonic

Chapter 7

Conclusion and further work

This thesis has presented different limited diffraction beams, and has shown that the different solutions are closely related. It has previously been shown that the Bessel beam and X wave can be well approximated by finite element, finite bandwidth and finite extent tranducers, and this thesis also shows that a good approximation to the X wave can be made on a small equal area annular array transducer.

The limited diffraction beams were then studied under nonlinear conditions, and it was shown that the second harmonic beamprofile was not as good as expected for small transducers, due to generation of high extra side-lobes. A larger aperture showed a better second harmonic profile, but is of less practical interest for ultrasound imaging. A modification of the beams was then shown to give good second harmonic properties for a large distance. The modified beams are not what would be termed limited diffraction beams, because they do not have equal focus through the depth of field, but tend to get broader as the propagation distance increases.

Further studies would be of interest for all areas covered by this thesis. Methods for sidelobe reduction for Bessel beams and X waves including higher order beams have been studied by Lu *et. al* [20], [21]. These methods require two-dimensional transducers as the higher order beams are no longer circular symmetric. Lu *et. al* [22], [23] also study steering of limited diffraction beams with two-dimensional array transducers, including a method to keep the effective aperture size equal when scanning different angles. Lu [24] proposes use of X waves on reception for high framerate 2D and 3D imaging and shows results from simulations. This method transmits a broadband plane wave and the incoming reflections are shaded by a sum of higher order X waves, resulting in a 3D image with only one transmitted beam.

Regarding nonlinear propagation, making the algorithm handle general geometries including linear and two-dimensional arrays is desirable. An idea

is to replace the discrete Hankel transform by a two-dimensional fast Fourier transform to avoid the limitations of the DHT. This however, adds a dimension to the transform, and would be very time consuming if a large number of harmonics must be included. Beams generated by practical transducers, which have good second harmonic properties including depth-independent focus, are still to be developed, and is an area where further research would be of interest.

Bibliography

[1] S. Holm, "Ultralydteknikker," *Fra Fysikkens Verden*, no. 3, 1998.

[2] D. H. Johnson and D. E. Dudgeon, *Array Signal Processing, concepts and techniques*. Prentice Hall, 1993.

[3] J.-Y. Lu, H. Zou, and J. F. Greenleaf, "Biomedical ultrasound beamforming," *Ultrasound Med. Biol.*, vol. 20, no. 5, pp. 403–428, 1994.

[4] E. G. Williams and J. D. Maynard, "Numerical evaluation of the Rayleigh integral for planar radiators using the FFT," *J. Acoust. Soc. Amer*, vol. 72, pp. 2020–2030, December 1982.

[5] J. A. Goodman, *Introduction to Fourier Optics*. McGraw-Hill, New York, 1968.

[6] H. F. Johnson, "An improved method for computing a discrete Hankel transform," *Comp. Phys. Comm.*, vol. 43, pp. 181–202, 1987.

[7] P. T. Christopher and K. J. Parker, "New approaches to the linear propagation of acoustic fields," *J. Acoust. Soc. Amer*, vol. 90, pp. 507–521, July 1991.

[8] J.-Y. Lu and J. F. Greenleaf, "Nondiffracting X waves - exact solutions to free-space scalar wave equation and their finite aperture realizations," *IEEE Trans. Ultrason., Ferroelect., Freq. Contr.*, vol. 39, pp. 19–31, Jan. 1992.

[9] S. Holm, "Bessel and conical beams and approximation with annular arrays," *IEEE Trans. Ultrason., Ferroelect., Freq. Contr.*, May 1998.

[10] J. Durnin, "Exact solutions for nondiffracting beams. I. The scalar theory," *J. Opt. Soc. Amer.*, vol. 4, pp. 651–654, Apr. 1987.

[11] J.-Y. Lu and J. F. Greenleaf, "Ultrasonic nondiffracting transducer for medical imaging," *IEEE Trans. Ultrason., Ferroelect., Freq. Contr.*, vol. 37, pp. 438–447, Sept. 1990.

[12] G. H. Jamshidi, "Limited diffraction beams," *Cand. Scient. thesis, University of Oslo, Dept. of Informatics*, 1997.

[13] S. Holm and G. Hossein Jamshidi, "Approximation of Bessel beams with annular arrays," in *Proc. IEEE Ultrason. Symp.*, (San Antonio, TX), pp. 881–884, Nov. 1996.

[14] J.-Y. Lu and J. F. Greenleaf, "Experimental verification of nondiffracting x waves," *IEEE Trans. Ultrason., Ferroelect., Freq. Contr.*, vol. 39, May 1992.

[15] S. Makarov and M. Ochmann, "Nonlinear and thermoviscous phenomena in acoustics, part 1," *ACUSTICA*, vol. 82, pp. 579–606, 1996.

[16] S. Makarov and M. Ochmann, "Nonlinear and thermoviscous phenomena in acoustics, part 2," *ACUSTICA*, vol. 83, pp. 197–222, 1997.

[17] P. T. Christopher and K. J. Parker, "New approaches to nonlinear diffractive field propagation," *J. Acoust. Soc. Amer*, vol. 90, pp. 488–499, July 1991.

[18] American Institute of Ultrasound in Medicine, National Electrical Manufacturers Association, *Standard for Real-Time Display of Thermal and Mechanical Acoustic Output Indices on Diagnostic Ultrasound Equipment*. American Institute of Ultrasound in Medicine, National Electrical Manufacturers Association, 1992.

[19] J.-Y. Lu and J. F. Greenleaf, "Effect on J_0 nondiffracting beam of deleting central elements of J_0 annular array transducer," *Ultrason. Imaging 13:203*, 1991 (Abs.).

[20] J.-Y. Lu and J. F. Greenleaf, "A study of sidelobe reduction for limited diffraction beams," *IEEE 1993 Ultrasonic symposium*, pp. 1077–1082, 1993.

[21] J.-Y. Lu and J. F. Greenleaf, "Sidelobe reduction for limited diffraction pulse-echo systems," *IEEE Trans. Ultrason., Ferroelect., Freq. Contr.*, vol. 40, pp. 735–746, Nov. 1993.

[22] J.-Y. Lu and J. F. Greenleaf, "Steering of limited diffraction beams with a two-dimensional array transducer," *IEEE 1992 Ultrasonics Symposium*, pp. 603–607, 1992.

[23] J.-Y. Lu and J. F. Greenleaf, "A study of two-dimensional array transducers for limited diffraction beams," *IEEE Trans. Ultrason., Ferroelect., Freq. Contr.*, vol. 41, pp. 724–739, Sept. 1994.

[24] J.-Y. Lu, "2D and 3D high frame rate imaging with limited diffraction beams," *IEEE Trans. Ultrason., Ferroelect., Freq. Contr.*, vol. 44, pp. 839–856, July 1997.

Appendix A

Matlab code

Algorithms for computing the results in this thesis were written in Matlab 4. Part of the code has been included here.

A.1   Discrete Hankel transform

A.1.1   Forward transform

```
function H = rft(h, Y, J, T)
%% Discrete Rotational Fourier Transform
%% (Discrete Hankel Transform)
%%
%% Returns the discrete Hankel transform of h
%%
%% h - Samples to transform
%% Y - Look-up table
%% J - Bessel zeros
%% T - Spatial extent (lateral) of acoustic field

N=length(h);
H=zeros(1,N);

for m = 1:N
        H(m) = sum(Y(m,1:N).*h');
end
H = H * 2*pi*T*T / (J(N+1)*J(N+1));
```

A.1.2   Backward transform

```
function h = irft(H, Y, J, T)
%% Inverse Discrete Rotational Fourier Transform
%% (Inverse Discrete Hankel Transform)
%%
%% Returns the inverse discrete Hankel transform of H
%%
%% H - Discrete Hankel transform
%% Y - Look-up table
%% J - Bessel zeros
%% T - Spatial extent (lateral) of acoustic field

N=length(H);
h=size(N,1);

for i = 1:N
        h(i) = sum(Y(i,1:N).*H);
end
h = h * 1/(2*pi*T*T);
```

A.2   Wave propagation

A.2.1   Linear wave propagation

```
function gg = linproprft(f0,c,N,M,T,x,obs,dz,z,t,s,Y,J)
%% returns acoustic field at distance z
%%
%% f0 - fundamental frequency
%% c - speed of sound
%% N - # lateral samples
%% M - # Fourier coefficients
%% x - intial field (normal velocity amplitude)
%% T - the acoustic fields spatial extent
%% obs - observation ..
%% ('lateral', 'axial','plane', 'axial-time', 'plane-time')
%% dz - stepsize for multistep propagation ('axial', 'plane')
%% z - observation plane / max axial distance for multistep propagation
%% t - observation time (if broadband wave)
%% s - peak of pulse center (cos(Axicon angle))
%% Y, J - discrete Hankel transform tables
```

```
%% ...
%% (only part of the algorithm is shown here
%% This part propagates the field in steps of length dz
%% to the maximum distance z)
%%


w0=2*pi*f0;
k0=w0/c;

X = rft2(x,Y,J,T);

l=0;
while l*dz < z
        l=l+1

        %% Calculate reponse function
        h = hresp(l*dz, M, N, k0, J, T, c);
        H = rft2(h, Y, J, T);

        G=X.*H;
        g=irft2(G, Y, J, T);
        if M > 1
        %% include time dependence if pulsed excitation

                t=l*dz*s/c;
                zum=0;
                for k=1:M
                        zum=zum+g(k,:)*exp(-j*(2*pi*f0/M)*k*t);
                end
                gg(l,:)=zum;
        else
                gg(l,:) = g(1,:);
        end
end
```

A.2.2   Nonlinear wave propagation

Multistep RFSC algorithm

```
function [g1,g2,g3] = nonlinproprft(f0,c,N,M,T,obs, ..
                x,dz,z,beta,tc,s,Y,J)
%% returns acoustic field
%%
%% f0 - maxium frequency (M*fundamental frequency)
%% c - speed of sound
%% N - # lateral samples
%% M - # Fourier coefficients
%% x - intial field (normal velocity amplitude)
%% T - the acoustic fields spatial extent
%% obs - observation ..
%% ('lateral', 'axial','plane', 'axial-time', 'plane-time')
%% dz - stepsize for multistep propagation ('axial', 'plane')
%% z - observation plane ('lateral') / max axial distance
%% beta - nonlinearity parameter (beta = 1 + B/2A)
%% tc - observation time (if broadband wave)
%% s - peak of pulse center (cos(Axicon angle))
%% Y, J - discrecte Hankel transform tables

k0=2*pi*f0/c;



%% Calculate response function

kn = k0/M:k0/M:k0; kn=kn'; H=zeros(M,N);

for i = 1:M
   for m = 1:N
      R(m) = J(m)/(2*pi*T);
      fn = kn(i)/(2*pi)*sin(atan((T)/dz));

      if R(m) <=fn;
         H(i,m) = exp(j*2*pi*dz*sqrt((kn(i)/(2*pi))^2 ..
                     - R(m)*R(m)));
      end
   end
end
```

```
G= rft2(x, Y, J, T);

%% Used for X waves
k=(1:M)';
kl=(1:M/2)';
kh=(M/2:M)';

for l=1:z/dz

   G = G.*H;
   g = irft2(G, Y, J, T);

   g = nonlinstep(g, dz, M, N, f0/M, c, beta);
   G = rft2(g, Y, J, T);

   t = l*dz*s/c;

   B1(l,:) = g(1,:);
   B2(l,:) = g(2,:);
   B3(l,:) = g(3,:);


   if strcmp(obs,'X');      %% If X wave simulation

       for i=1:N

           B1(l,i) = sum(g(kl,i).*exp(-j*(2*pi*f0/M)*kl*t));
           B2(l,i) = sum(g(kh,i).*exp(-j*(2*pi*f0/M)*kh*t));
           B3(l,i) = sum(g(:,i).*exp(-j*(2*pi*f0/(M))*k*t));
       end
   end

   %% Truncate H before the next step according to ray theory;
   for i = 1:M
       for m = 1:N
           R(m) = J(m)/(2*pi*T);
           fn = kn(i)/(2*pi)*sin(atan((T)/((l+1)*dz)));

           if R(m) > fn;
               H(i,m)=0;
```

```matlab
        end
      end
   end
end

%% Converting to acoustic pressure
g1 = B1*c/10^3;
g2 = B2*c/10^3;
g3 = B3*c/10^3;

if strcmp(obs,'plane-time')  %% If snapshot in time
   zum=0; I=length(t); gg=zeros(I,N);
   for i=1:N
       for n=1:length(tc)
           g1(n,i) = sum(g(kl,i).*exp(-j*(2*pi*f0/M)*kl*tc(n)));
           g2(n,i) = sum(g(kh,i).*exp(-j*(2*pi*f0/M)*kh*tc(n)));
           g3(n,i) = sum(g(k,i).*exp(-j*(2*pi*f0/M)*k*tc(n)));
       end
   end;
   g1 = g1*c/10^3;
   g2 = g2*c/10^3;
   g3 = g3*c/10^3;

end
```

Nonlinear step

```matlab
function u = nonlinstep(x, dz, M, N, f, c, beta);
%% x = acoustic field after linear step
%% dz = length of linear/nonlinear step
%% M = number of Fourier-coefficients
%% N = number of spatial samples
%% f = fundamental frequency
%% c = speed of sound

for n=1:M
        zum1=zeros(1,N); zum2=zeros(1,N);
        for k=1:n-1
                zum1 = zum1 + k*x(k,:).*(x(n-k,:));
        end
        for k=n+1:M      %% No zeroth harmonic
```

```
                zum2 = zum2 + n*x(k,:).*conj(x(k-n,:));
        end

        u(n, :) = x(n, :) + ..
                j*beta*pi*f*dz/(2*c*c)*(zum1 + zum2);
end
```